Active faults in the Anatolian-Aegean plate boundary region with Nubia

Ali Değer ÖZBAKIR[1,2,*], Rob GOVERS[1], Rinus WORTEL[1]
[1]Department of Earth Sciences, Utrecht University, Utrecht, the Netherlands
[2]Kandilli Observatory and Earthquake Research Institute, Boğaziçi University, Çengelköy, İstanbul, Turkey

Abstract: Convergence of the Africa, Arabia, and Eurasia plates and the westward escape of Anatolia have resulted in an evolving plate boundary zone in the Eastern Mediterranean. The current location and nature of the plate boundary between the Anatolian and the African plate is difficult to trace due to the scattered crustal earthquakes and the absence of deep ones. We examine various types and locations for the plate boundary as constrained by seismicity, seismic reflection studies, tomographic studies, and geodetic measurements and we use a spherical plane stress finite element model to test these possibilities. In our regional model, we impose the convergence of Africa, Arabia, and stable Eurasia by applying GPS-derived velocities in the far-field, as well as the roll-back of the Hellenic trench to solve for regional deformation. Model velocity and stress fields are compared with GPS-derived velocities and stress directions from focal mechanism solutions. We find that the plate boundary via the Pliny and Strabo trenches, the Anaximander Mountains, the Eratosthenes Seamount collisional segment, and the Latakia-Larnaka ridges gives the best fit to the data. The Anaximander Mountains plate boundary has both down-dip and strike-slip motions, and the Latakia segment is pure strike-slip. The Cyprus subduction contact is 42% locked. From a combined analysis of indicators for long-term deformation (predominantly slip-rates on major faults) and model results we infer that this southern plate boundary configuration may have existed since the Late Pliocene.

Key words: Space geodetic surveys, kinematics of crustal deformation, finite element modeling, stress and velocity field of the Anatolia-Aegean region, NAF slip-rates

1. Introduction

The Anatolian-Aegean region is located in the zone of convergence between the Africa, Arabia, and Eurasia plates (McKenzie, 1972) (Figure 1). Essentially, the Anatolian-Aegean region has come into existence by the accretion of (semi-)rigid blocks to the southern margin of the Eurasian plate and it has undergone intense deformation. Presently, Anatolia moves westwards with respect to stable Eurasia (Ketin, 1948), from the Arabia collision zone in eastern Turkey and the Zagros region towards the Hellenic subduction zone to the southwest. Some of the regional plate boundaries are well defined: the North Anatolian Fault (NAF) accommodates the motion of Anatolia relative to Eurasia, and the East Anatolian Fault (EAF) accommodates the motion relative to Arabia (McKenzie, 1976; McClusky et al., 2000). The plate boundary along the Hellenic arc is well defined in western Greece, south of the Peloponnese and Crete (Taymaz et al., 1990; Baker et al., 1997; Shaw and Jackson, 2010).

Özbakır et al. (2013) recently proposed that the Pliny and Strabo trenches in the eastern part of the Hellenic arc represent the surface expression of a STEP type of plate boundary (Govers and Wortel, 2005), as such referred to as a STEP *fault* (Baes et al., 2011), which is the boundary zone between the nonsubducted African lithosphere and the Aegean lithosphere that overrides the subducted Aegean slab. Continual tear faulting of the African lithosphere at the active STEP separates the subducting lithosphere from the lithosphere at the surface. It was shown that the surface geology documents both strike-slip and convergent tectonics in accordance with a Tchalenko (1970) sinistral shear zone model. The Africa-Aegean velocity component perpendicular to the Pliny-Strabo shear zone was proposed to be accommodated by the Rhodes fold and thrust belt: the outboard part of the Rhodes Basin consists of a broad NE–SW trending strike-slip zone with predominant compression inferred from kilometer scale thrust relief (Hall et al., 2009) and superficial extension (Ten Veen et al., 2004). Although the Pliny-Strabo trenches thus have a small component of convergence on them, most of the relative motion since the Pliocene has been strike-slip (Reilinger et al., 2006; Vernant et al., 2014).

Farther to the east, between Rhodes and Cyprus, the plate boundary is obscure. The broad geographical
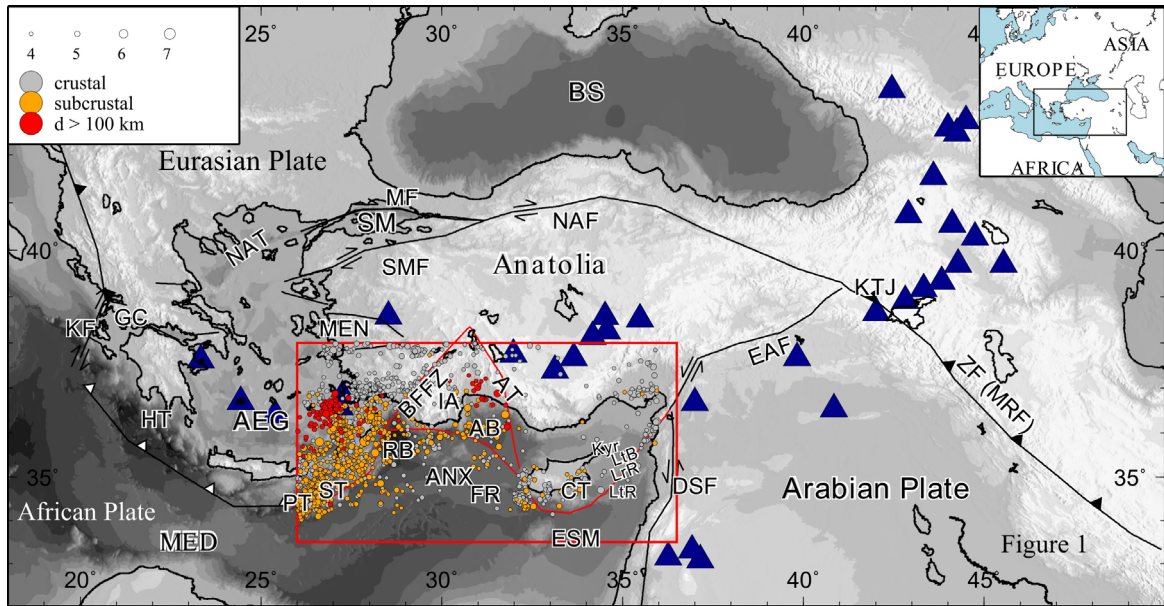
* Correspondence: aozbakir@gmail.com

Figure 1. Tectonic setting of the Eastern Mediterranean. We mainly focus on the location and nature of (possible) plate boundaries (red line segments) in the boxed region. Triangles on faults with black and white filling indicate collision and subduction zones, respectively. Conjugate arrows indicate the strike-slip character of faults; normal faults have no additional labels. Seismicity in the box is shown for the period of 1973–2009 (NEIC, http://neic.usgs.gov/neis/epic/index.html). The distinction between crustal and subcrustal earthquakes is based on the Moho depth map of Grad et al. (2009). Loci of subcrustal and deep seismicity are Hellenic and Cyprus trenches. Blue triangles indicate active volcanism. Abbreviations: AB, Antalya Basin; AEG, Aegean Sea; ANX, Anaximander Mountains; AT, Aksu Thrust; BFFZ, Burdur Fethiye Fault Zone; BS, Black Sea; CT, Cyprus Trench; DSF, Dead Sea Fault; EAF, East Anatolian Fault; ESM, Eratosthenes Seamount; FR, Florence Rise; GC, Gulf of Corinth; HT, Hellenic Trench; IA, Isparta Angle; KF, Kephalonia Fault; KTJ, Karlıova Triple Junction; Kyr, Kyrenia Ridge; LrT, Larnaka Ridge; LtB, Latakia Basin; LtR, Latakia Ridge; MED, Mediterranean Sea; MEN, Menderes Massif; MF, Marmara Fault; NAF, North Anatolian Fault; NAT, North Aegean Through; PT, Pliny trench; SM, Sea of Marmara; SMF, Southern Marmara Fault; ST, Strabo Trench; ZF, Zagros Fault (Main Recent Fault).

distribution of earthquakes, lack of deep earthquakes, and discontinuous arc volcanism belonging to the subducting African lithosphere (Figure 1) contribute to this uncertainty. In addition, the large separation of GPS stations at opposite sides of the possible plate boundary zone precludes the delineation of this boundary (Figure 2A). In short, the location and nature of the plate boundary between Rhodes and Cyprus is unknown. This is the main topic of this paper.

Earthquake epicenters between the longitudes of Rhodes and Cyprus are distributed along bathymetrical highs, basins, and faults, both offshore and onshore, which present potential features to be associated with a plate boundary (red lines in Figure 1). These features are the Burdur–Fethiye fault zone (BFFZ), Aksu Thrust (AT), Rhodes basin (RB), Anaximander Mountains (AM), and Florence Rise, which define the margins of a complex tectonic zone known as the Isparta Angle (IA) (Figure 1).

The BFFZ constitutes the western limb of the Isparta Angle and it was interpreted as a left-lateral strike-slip fault zone by Price and Scott (1994), Eyidoğan and Barka (1996),

and, more recently, Hall et al. (2014). Alternatively, the BFFZ is interpreted as a normal fault zone (Koçyiğit, 2000; Alçiçek et al., 2006) without significant strike-slip motion (Kaymakçı et al., 2014). Earthquake focal mechanisms do indeed not support a strike-slip interpretation (Taymaz and Price, 1992), but this may still agree with a STEP fault: relative motions further away from the active STEP can be zero – this is an aspect that is particular to this type of plate boundary and distinguishes it from a transform fault (Govers and Wortel, 2005). Barka and Reilinger (1997) considered the BFFZ as the on-land extension of the Pliny-Strabo trenches on the basis of the coherence of earthquake slip and GPS-derived velocity vectors. Hall et al. (2009, 2014) interpreted offshore seismic reflection data in combination with on-land geology as supporting the connection of the Pliny-Strabo trenches to the BFFZ. Basin and fault analyses near the fault zone indicate that the sinistral motion of the Pliny-Strabo trenches penetrates the southwestern tip of the BFFZ (Alçiçek et al., 2006). The eastern boundary of the Isparta Angle is defined by the Sultan Dağ Thrust (Boray et al., 1985), but the majority
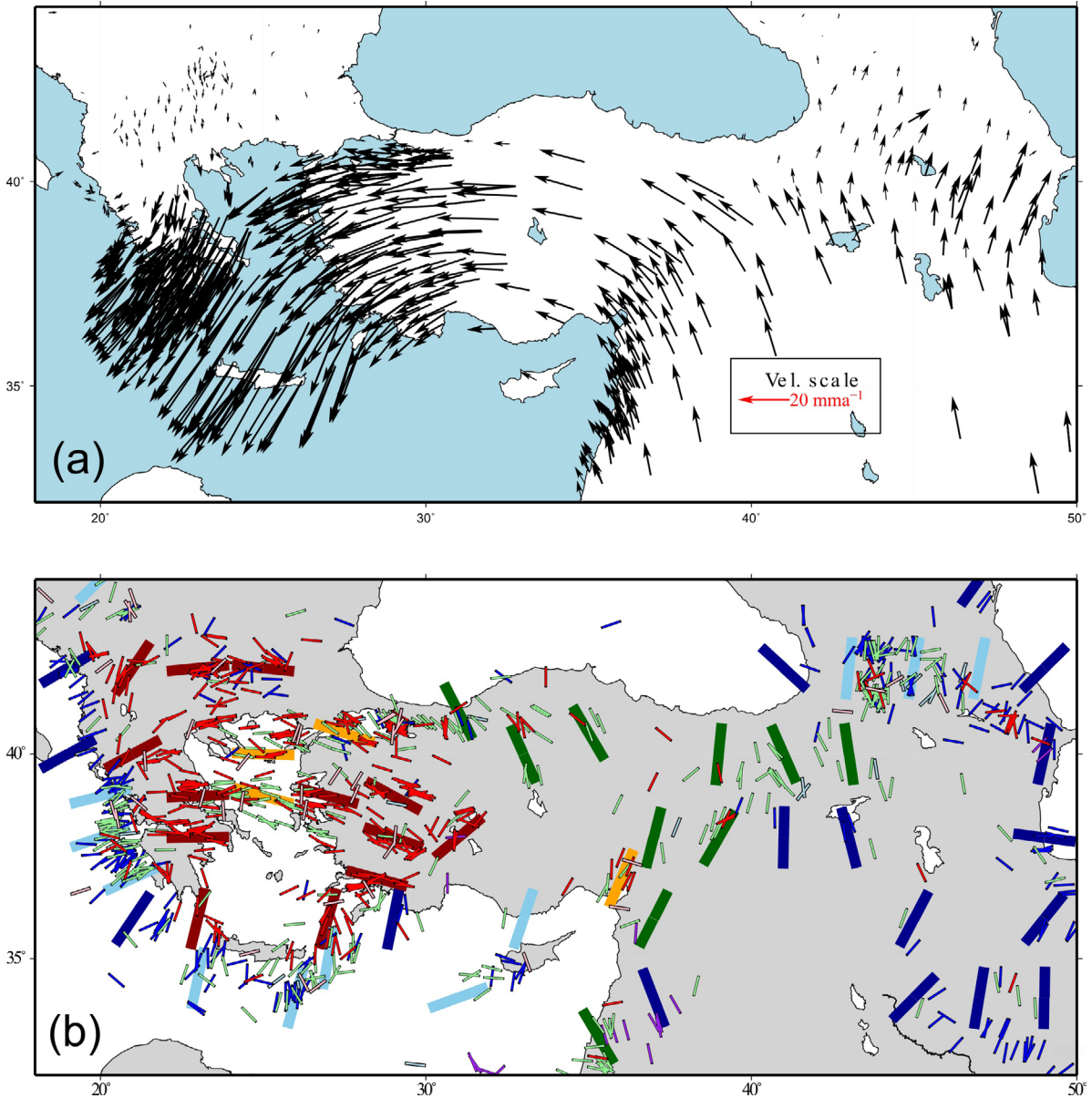
Figure 2. a) Compilation of GPS velocities (Burchfiel et al., 2006; Hessami et al., 2006; Kotzev et al., 2006; Masson et al., 2006; Reilinger et al., 2006; Hollenstein et al., 2008; Aktuğ et al., 2009; Alchalbi et al., 2010; Floyd et al., 2010). b) "Observed" horizontal stress directions. Bars indicate the direction of maximum compression. Thin bars are taken from the World Stress Map project (Heidbach et al., 2008). Color indicates the stress regime: dark blue for thrusting, light blue for oblique thrusting, green for strike-slip, orange for oblique tension, and red for tension. Wide bars represent spatial averages of the maximum horizontal stress axis, computed with the method of Mardia (1972).

of seismic activity is under the Aksu Thrust. Zitter et al. (2003) inferred the continuity of the western limb of the Cyprus arc with the Isparta Angle from imaging similar fault types and trends. The first possible plate boundary thus follows the northern perimeter of the Isparta Angle (Figure 1).

Another possible location for the plate boundary follows from considering the region south of the Turkish mainland, where bathymetric trends and faults of the Pliny trench have strikes similar to that of the Turkish continental slope (ten Veen et al., 2004). Furthermore, the post-Miocene deformation age of the Pliny trench also correlates well with the Finike basin, which is located between the Anaximander Mountains and the Turkish continental slope (ten Veen et al., 2004). This led ten Veen et al. (2004) to propose that the Pliny trench connects with

the faults to the north of the Anaximander Mountains. Consistent with this interpretation, Ocakoğlu (2012) found evidence in swath bathymetry and seismic data that the BFFZ and the Pliny-Strabo "trench" system represent different fault systems. Ten Veen et al. (2004) interpreted the Anaximander Mountains as a broad sinistral shear zone. The Florence Rise is the broad bathymetrical high to the southeast of the Anaximander Mountains and it separates the Antalya Basin from the region of convergence to the south and southwest (Woodside et al., 2002). Shallow marine seismics (Aksu et al., 2009) show NW-SE trending thrust faults with similar vergences in the region between the Anaximander Mountains and the Florence Rise. This suggests that the present-day plate boundary between Rhodes and Cyprus is located offshore, to the south of Anatolia (Wdowinski et al., 2006).

P-wave tomography under the Isparta Angle region outlines the subducted African plate and the Anatolian lithosphere (Biryol et al., 2011). However, tomographic resolution is insufficient at shallow levels to identify which of the two above alternatives is the plate boundary: near the surface, the boundary zone closely follows the trend of the Strabo "trench", Anaximander Mountains, and Florence Rise. The boundary of the "Western Cyprus Slab" seismic velocity anomaly roughly corresponds to near-surface features such as the Antalya Bay, Aksu Thrust, BFFZ, and Pliny trench (figures 9 and 10 in Biryol et al., 2011), which may also be the plate boundary.

Thus, for the Rhodes-Cyprus segment two possible plate boundaries can be hypothesized (Figure 1): one follows the Aksu Thrust and the BFFZ, forming the outer Isparta Angle, and the other follows the Anaximander Mountains and Antalya Bay. Hereafter, we refer to the boundary along the outer Isparta Angle as NORTH and to the one following the Anaximander Mountains as SOUTH. Our aim is to constrain the location and nature of the plate boundary that is shown with thick red lines in Figure 1, and to evaluate for how long approximately this plate boundary has been active.

The two plate boundary configurations have a common segment from the south of Cyprus towards the east. Here, the Eratosthenes Seamount (ESM), a continental fragment on the African plate, is in the process of colliding with the Cyprus arc (Ben-Avraham et al., 1988; Robertson, 1998; Mascle et al., 2000). The degree of coupling between the African plate and Anatolia along the ESM plate boundary segment, however, is not known.

The easternmost segment of the Cyprus arc is composed of a linked fault-and-thrust belt with intervening basins extending to the Levant coast: the Troodos Larnaka culmination in the south and the Kyrenia belt to the north, with the intervening Latakia basin constituting the foreland of the Tauride system (Aksu et al., 2005; Calon et al., 2005). The transition from the Eratosthenes collision zone to a transtensional regime in the Latakia-Larnaka segment was inferred from shallow seismic reflection studies (Vidal et al., 2000). Although the location of this part of the plate boundary between Africa and Anatolia is well constrained, its nature is not.

Our approach is based on the understanding that forces exerted at plate boundaries shape the stress field and, in combination with the rheology, the deformation of the lithosphere (e.g., Warners-Ruckstuhl et al., 2012, 2013) with the plate boundaries' location naturally giving the distribution of the forces involved, the plate boundaries' nature determines their direction and magnitude. We therefore step back and consider Anatolia to be part of a deformation zone with finite discontinuities (plate boundaries and faults) and a north-south extent of hundreds of kilometers. We use mechanical models with either the NORTH or the SOUTH plate boundary geometry to predict the velocity field in Anatolia for comparison with available GPS velocity data. Active faults within Anatolia have been mapped based on their morphological and seismic expressions (Bozkurt, 2001; Emre et al., 2013). Significant fault slip is possible only on the major fault zones. We therefore will evaluate the improvement in the model compatibility with the GPS-derived velocities when we incorporate these major faults (or shear zones).

The first part of this study deals with the present day and the aim is to determine the preferred southern plate boundary configuration for the present. In the second part we use indicators for the long-term deformation (slip-rates on major faults over many seismic cycles and paleomagnetic rotations) to study the stability of this plate boundary in recent geological time.

2. Modeling approach

For modeling the Anatolian-Aegean deformation two end-members for the rheology can be assumed. One considers a strong continental lithosphere and assumes the motion of crustal/lithospheric blocks to be coupled through narrow shear zones (e.g., Nyst and Thatcher, 2004; Reilinger et al., 2006; Floyd et al., 2010). The other considers the continental lithosphere to be weak and models it as a thin viscous sheet (e.g., Cianetti et al., 2001; Jimenez-Munt et al., 2003; Özeren and Holt, 2010) or an elastic-plastic crust with a viscous mantle (Fischer, 2006). The former method is known as the block modeling approach, whereas the latter is collectively known as the continuum approach.

Block models are based on rigid crustal blocks that are fully enclosed by faults. They have been successful in describing the surface velocity field with high accuracy and enable calculation of slip-rates on active block bounding faults. However, neither the assumption of an undeforming

block nor that of complete closure of the bounding faults appears to be realistic. In most regions that are studied using block models, some parts of the block boundaries are not expressed in the geology, meaning that they have little meaning on time scales of multiple earthquake cycles.

Continuum models are based on the assumption that crustal/lithospheric regions between faults are mechanically weaker than the faults themselves, e.g., thin viscous sheet models (England and McKenzie, 1982). Continuum models relate driving forces (e.g., ridge push, slab pull, gravitational body forces, trench suction) to deformation by varying rheology (Thatcher, 2009). Offsets along plate boundaries and major faults in Anatolia show a significant fraction of the faults and shear zones are as weak as, or weaker than, the rocks separating them. We therefore think that continuum models are not geologically realistic.

Loveless and Meade (2011) presented an elegant methodology that seeks to combine the two perspectives/ approaches. They inverted GPS observations to find slip on (predefined) block boundaries and block deformation. Our approach is similar in that we combine the strengths of both modeling approaches. It is different because we do not work with blocks that are fully enclosed by faults because geological observations do not support the existence of these in Anatolia. We only incorporate finite length faults that have been observed from the geology and active tectonics. We solve for stresses and deformation and try to find the minimum number of geologically inferred faults that is required by a given GPS dataset. We use an elastic rheology to capture the continuum deformation, which is consistent with the time scale of a few or more earthquake cycles (henceforth referred to as the geodetic time scale). Implicit in this approach is that deformation associated with small faults is represented by the continuum deformation. Similar to what is observed, e.g., near the eastern end of the Altyn Tagh fault in the Tibetan plateau, distributed deformation is expected here particularly.

3. Observations
3.1. GPS-derived velocity field
GPS-derived velocities are the main observational constraint in this study, primarily because of their (very high) accuracy and therefore their sensitivity to the location and nature of the plate boundary. Horizontal velocities have an accuracy of around 1 mm/year on average on a benchmark network with good coverage of the model domain.

In addition to the data from Reilinger et al. (2006), we use available GPS-derived velocity data for western Anatolia (Aktuğ et al., 2009), northwestern Arabia (Alchalbi et al., 2010), the western Hellenic Arc (Hollenstein et al., 2008),

Greece (Floyd et al., 2010), northern Iran (Masson et al., 2006), Zagros (Hessami et al., 2006), and Macedonia and western Bulgaria (Burchfiel et al., 2006; Kotzev et al., 2006) (see Figure 2a) for comparison with the modeled velocity. Reilinger et al. (2006) used measurements from before the 1999 İzmit (Mw = 7.4) earthquake, which are not affected by postseismic or coseismic effects. The measurements of Aktuğ et al. (2009), however, were collected after the 1999 İzmit and 1999 Düzce (Mw = 7.2) earthquakes. Aktuğ et al. (2009) identified the sites that were affected by postseismic and coseismic motions by comparing his velocity results with those of Reilinger et al. (2006). Hollenstein et al. (2008) used measurements before the Lefkada 2003 (Ms = 6.2), Skyros 2001 (Mw = 6.4), and Strofades 1997 (Ms = 6.4) earthquakes for the velocity calculations. Floyd et al. (2010) excluded sites that were affected by Mw ≥ 6 earthquakes during the observation period. Kotzev et al. (2006) corrected for the İzmit earthquake coseismic slip at the affected stations. Alchalbi et al. (2010), Masson et al. (2006), and Hessami et al. (2006) did not report of any earthquakes that affected their velocity determinations. Hence, we consider our combined dataset to be unaffected by coseismic and postseismic motions. The GPS velocities likely do reflect the impact of long-term locking of faults.

All velocities are specified in an ITRF2000 Eurasia-fixed reference frame. We did not correct the published velocities for relative network rotations. Discrepancies due to different network representations are a few millimeters per year in overlapping stations in the datasets, all of which are within the error ellipses. We removed data with larger standard deviations from the database for overlapping stations.

3.2. World Stress Map data
World Stress Map (WSM) data provide the direction of the largest horizontal compressive principal stress axis and the stress regime (Heidbach et al., 2008) (Figure 2b). Data from various sources and quality are compiled in the WSM. In our domain, 90% of the data were derived from focal mechanism solutions. On average, these are of C-grade quality, corresponding to a 25° angular error for the maximum compressive horizontal stress axis (SHmax). Therefore, WSM data are less accurate than the GPS data. We smoothed the WSM data using the method of Mardia (1972) for comparison with model stresses (see Heidbach et al. (2010) and Warners-Ruckstuhl et al. (2013) for a detailed explanation of the method). This method finds a smooth and continuous field of stress directions whose difference from observed stress directions is minimized. The choice of search radius does not significantly change the smoothed output field, but it results in lower uncertainties. The directions of maximum compressive stress thus obtained are shown with large bars in Figure 2b. A detailed plot for stress observations, smoothed stress field, and stress variances is given in Appendix A.

4. Model setup

We model the present-day secular velocity field of the Eastern Mediterranean with emphasis on the Anatolia-Aegean region. Since the horizontal extent of the domain is much larger than the vertical (model) dimensions, and because the data have little depth information, the 3D mechanical equilibrium equations can be simplified to 2D by assuming plane stress. We solve these equations with plane stress spherical finite element code GTECTON (Govers and Meijer, 2001).

4.1. Domain and rheology

The model domain, boundary conditions, and faults for the plate boundary configurations NORTH and SOUTH are shown in Figure 3. The lithosphere responds to
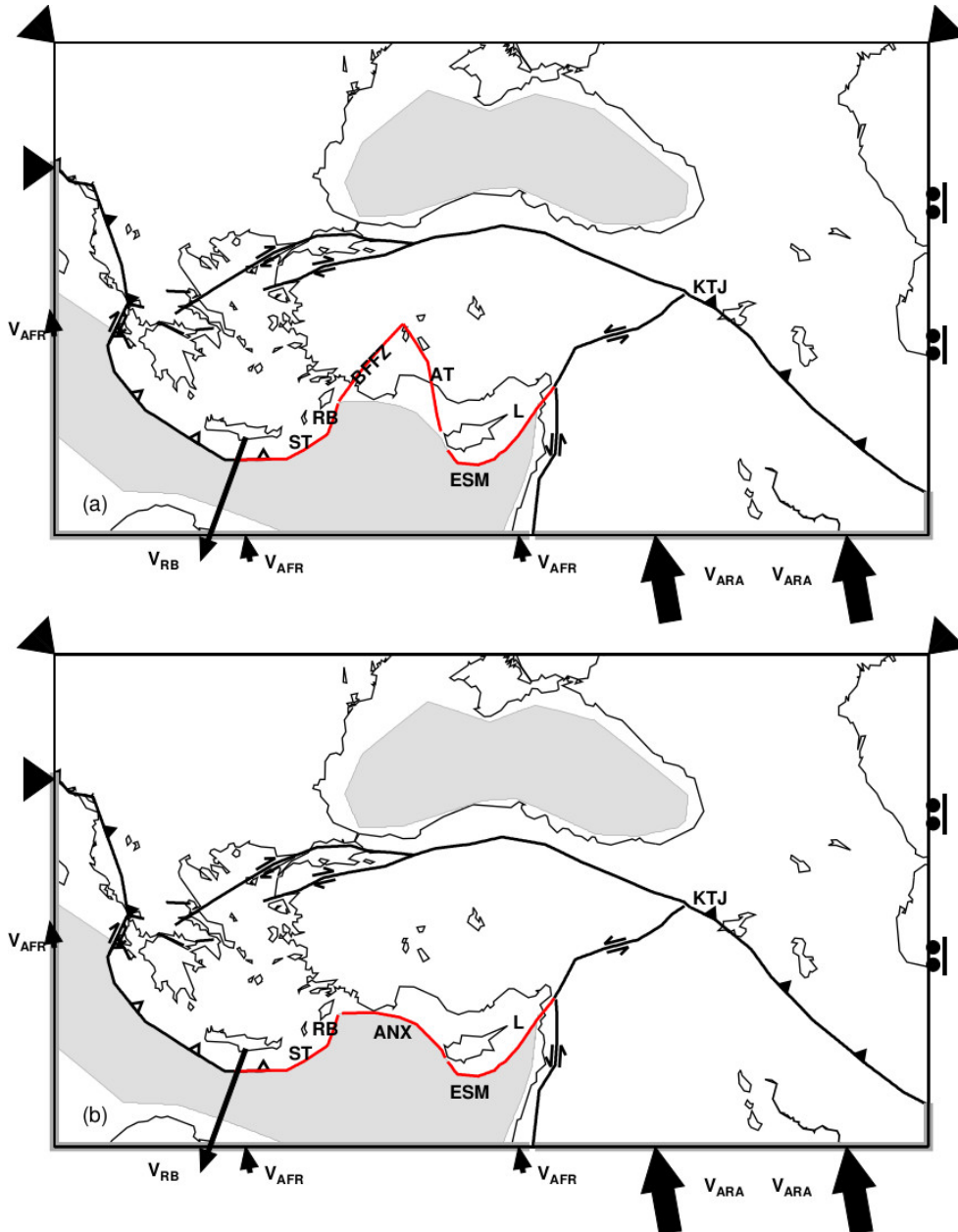

Figure 3. Model domain, boundary conditions, and known and unknown faults for (a) NORTH and (b) SOUTH model. Known faults are colored black with their sense of slip. Unknown faults are shown in red. The shaded region indicates oceanic lithosphere. GPS-derived velocities are imposed along the African and Arabian margins of the model (thick gray line along the plot frame): v_AFR and v_ARA. V_RB is the imposed differential velocity on the plate contact of the Hellenic subduction zone. Rollers on the east boundary correspond to the observation that GPS velocities are oriented approximately north-south here. Solid triangles along the north and NW boundary of the model indicate that here the model is fixed. Abbreviations are the same as in Figure 1.

stresses by elastic, brittle, or viscous deformation. Viscous deformation occurs on many time scales, but mostly on geological time scales. Within our study area significant lateral variations exist in the surface height and topology of the Moho (and other density interfaces). Gravity leads to horizontal forces acting where there are gradients in topography and/or Moho depth, i.e. the forces act in a distributed way rather than as a line force like we assumed in our (boundary-driven) models so far. As our analysis is based on the fit to surface deformation data, this difference between distributed and line forcing could potentially affect our conclusions significantly. We investigate to what extent our (simple) velocity-driven models correspond to (more realistic yet complicated) models driven by gradients in gravitational potential energy (GPE) in Appendix D.

For the first part of the paper we compare model results with geodetic velocities (acquired on time scales of years to decades). We therefore take the lithosphere to be elastic with faults. Our model domain encompasses both oceanic and continental lithosphere, which have different Young's moduli. In studies focusing on continental areas, Young's modulus values of 70–75 GPa (e.g., Meijer and Wortel, 1996, 1997; Lundgren et al., 1998; Plattner et al., 2009) and for oceanic areas 100–130 GPa (Watts and Zhong, 2000; Got et al., 2008) have been used. Therefore, we assign 75 GPa to continental Arabia, Africa, and Eurasia and use 100 GPa for the Black Sea and the Mediterranean. The Anatolian-Aegean region formed in a context of Cretaceous-Recent subduction of branches of the Neo-Tethys and accretion of intervening ribbon continents (Şengör and Yılmaz, 1981). The entire region is therefore mechanically weak and prone to large deformation. We conducted a priori sensitivity analysis using reference models (Section 5) with several different Young's moduli, and we select 25 GPa for the Anatolian-Aegean region. Poisson's ratio is assumed to be 0.3. We used convergence tests to verify that all results shown in this paper are insensitive to further refinement of the finite element grid.

4.2. Boundary conditions

The northern edge and the northwestern part of the model domain are located in stable Eurasia. As we take stable Eurasia as our reference frame, nodes along these domain edges are fixed in both horizontal directions. The eastern margin of the domain can move in a N-S direction, consistent with ongoing N-S strain in the Zagros and Caucasus (Allen et al., 2004). We force the system by applying GPS-derived velocities in the far-field, i.e. along domain edges in the African and Arabian plates (v_{ARA}) (Reilinger et al., 2006). We also impose the relative velocity at the Hellenic trench v_{RB} using the split node technique (Melosh and Raefsky, 1981): since observed relative velocities at the Hellenic trench represent the response to forces due to GPE, trench suction, slab pull,

sublithospheric mantle flow, and plate contact resistance, the imposed relative velocity at the trench implicitly accounts for the contribution of GPE forces (and other forces) to the regional kinematics. To avoid double forcing, we do not include body forces in these models.

In Section 6 we will present models with an alternate choice for the forcing. By their very nature, body forces (and GPE) act on volumes rather than at plate boundaries. In Section 6 we therefore will investigate to what extent our (simple) velocity-driven models correspond to (more complicated) GPE-driven models.

4.3. Plate boundaries and faults

Plate boundaries and principal (larger) faults are shown in Figure 1. The Dead Sea Fault (DSF) takes up the relative motion between the African and the Arabian Plates. The dextral NAF and the sinistral EAF accommodate westward extrusion of Anatolia. Coming from the east, the NAF bifurcates into two branches east of the Sea of Marmara (see Şengör et al., 2005 for a review). The main northern branch continues along the Sea of Marmara and enters the Aegean Sea. Across the North Aegean, the continuation of the NAF manifests itself as a broader shear zone and connects with central Greece via the North Aegean Trough (NAT) and the Sporades (Dewey and Şengör, 1979; Lyberis, 1984). The southern branch of the NAF in the Marmara region has a SW–NE strike and is composed of a set of discrete faults (Şengör et al., 2005). We represent these discrete faults in the model by a single, continuous fault zone. In the west, the Hellenic Arc terminates at the 150-km-wide dextral strike-slip zone including the Kephalonia Fault (KF), which marks the transition from oceanic subduction to continental collision (Baker et al., 1997; Shaw and Jackson, 2010). Following Özbakır et al. (2013), we implement the Pliny and Strabo trenches as a single shear zone. The Rhodes Basin consists of a broad NE–SW trending transpressive zone that has the characteristics of a fold and thrust belt (Hall et al., 2009). Therefore, we implement the fold and thrust belt as possibly accommodating both dip-slip and strike-slip motions. Further to the northeast, the Rhodes Fault links the Pliny and Strabo trenches to the Anaximander Mountains.

The selection of active faults in western Anatolia is based on two criteria: the scale of faults and the seismic activity on them. The argument of scale, more specifically, is the condition that the length of a fault is comparable to the crustal thickness in the region. Thus, faults shorter than the crustal thickness or aseismic mapped faults are not incorporated in our analysis. In the course of model development, we implemented some long fault traces such as the Simav fault and Gökova faults. Importantly, some of the fault strands in Western Anatolia are represented in our models as part of a longer fault system rather than by their individual segments. An example is the Bakırçay

graben. This graben or the Balıkesir and Havran fault zones are in fact long fault zones, which are included in our model as the southern branch of the NAF. Another example is Alaşehir graben, which is incorporated within the Burdur–Fethiye fault zone.

In our model, we control the nature of faults by a priori imposing whether slip is allowed in a fault parallel and/or fault normal direction. The "slippery node" formalism (Melosh and Williams, 1989) that we employ has the important property that dynamic stresses in the model determine whether or not such fault slip occurs. Strike-slip faults in the model are assumed to be vertical and frictionless, and fault motion is constrained to be fault-parallel; we do not impose the sense of relative motion. Thrust faults are assumed to be subhorizontal (~30 degrees) with both fault-normal and fault-parallel motion allowed. In the collision process, horizontal convergence causes an increase of topography. This uplift is controlled by the fault dip and by Airy isostasy: as the height of the orogen increases, the resistance to further growth of the topography increases. To represent this fault-normal resistance in our model, we adopt the formulation of Van Benthem and Govers (2010). Fault-parallel motion on thrust faults is taken to be frictionless. Extensional faults are implemented by only allowing fault-normal motion. Triple junctions are represented by triple overlapping nodes (Plattner et al., 2009).

4.4. Model evaluation

To quantify the misfit between modeled and observed velocity fields we use the reduced chi-square statistic defined here as:

$$\chi_R^2 \stackrel{\text{def}}{=} \frac{1}{N - n_T - 1} \sum_{i=0}^{N} \left(\frac{(v_i^{o,x} - v_i^{m,x})^2}{\sigma_i^{x\,2}} + \frac{(v_i^{o,y} - v_i^{m,y})^2}{\sigma_i^{y\,2}} \right)$$

v_i^c and v_i^m are observed and modeled horizontal velocities at GPS station number i and subscripts x, y denote easting and northing components of the velocity vector. N is the number of observations, n_T is the number of model elements, and σ_i is the error in the GPS velocity. The number of model elements is the total number of degrees of freedom on model faults, determined as follows. When a fault segment is locked, it has zero degrees of freedom. When a fault segment is allowed to move in one direction (strike-slip, pure normal, or dip-slip), it has one degree of freedom. When a fault segment can move in both strike-slip and dip-slip directions, it has two degrees of freedom. In principle, a large X_R^2 represents a poor fit. Scaling by one over $N-n_T-1$ has the consequence that, when two models have the same sum of squares, X_R^2 will be smaller for the model with fewer constraints n_T, i.e. the simpler model. The reduced chi-square statistic thus has the desired

property of favoring the simpler over the more complex model when looking for the lowest value. Degrees of freedom (DOFs) of model faults are represented by open/filled triangles and strike-slip symbols in Figures 4 and 5. Open triangles show the case where both strike-slip and normal motion is allowed. Filled triangles indicate that only motion perpendicular to the fault strike is allowed, and strike-slip symbols indicate that fault parallel motion is allowed; here, the sense of motion indicated by the strike-slip symbols is meaningless, because this is a model result, not a priori imposed.

5. Model results and analysis
5.1. NORTH or SOUTH

In this section, we present model results for the NORTH and SOUTH plate boundary scenarios. We first present two "reference models" based on accepted regional plate boundaries and the two plate boundary scenarios (Figure 3). As discussed below, the difference between modeled and observed velocities is larger than the data error in these models. Therefore, we will proceed with more complex models to study how the introduction of additional faults affects the fit to the observations. Importantly, we only introduce faults with clear geological expressions.

5.1.1. Reference models NORTH and SOUTH

The NNW-directed motion of Africa towards Anatolia decomposes into plate boundary parallel and normal components. As a starting point, we therefore define reference models where both down-dip and fault parallel motions are allowed along plate boundaries NORTH and SOUTH. Model velocity fields of the reference models are shown in Figures 4a and 4b. The overall pattern is similar to the GPS observations shown in Figure 2a: an increase in the velocity from east to west in a counter-clockwise pattern around a pivot in Cyprus. The difference between the observed and modeled velocity vectors, hereafter referred to as the "residual velocity" vectors or "misfits", gives a better indication of the sensitivity of the velocity field to changes in the unknown faults' nature and geometry. These residual velocities are plotted with black vectors on the misfit maps (Figures 4c and 4d). The other useful quantity is the fault slip-rate, which shows the direction and magnitude of fault motion in the model. Slip-rates are calculated with respect to the Anatolian-Aegean region and are shown by blue vectors for each of the scenarios.

Both reference models explain the observations in the Arabian plate within confidence limits. Other parts of the eastern model domain show significant misfits, notably in easternmost Turkey, Armenia, and Azerbaijan. A likely reason for this is the uniform free-slip boundary condition on the eastern boundary of the model domain
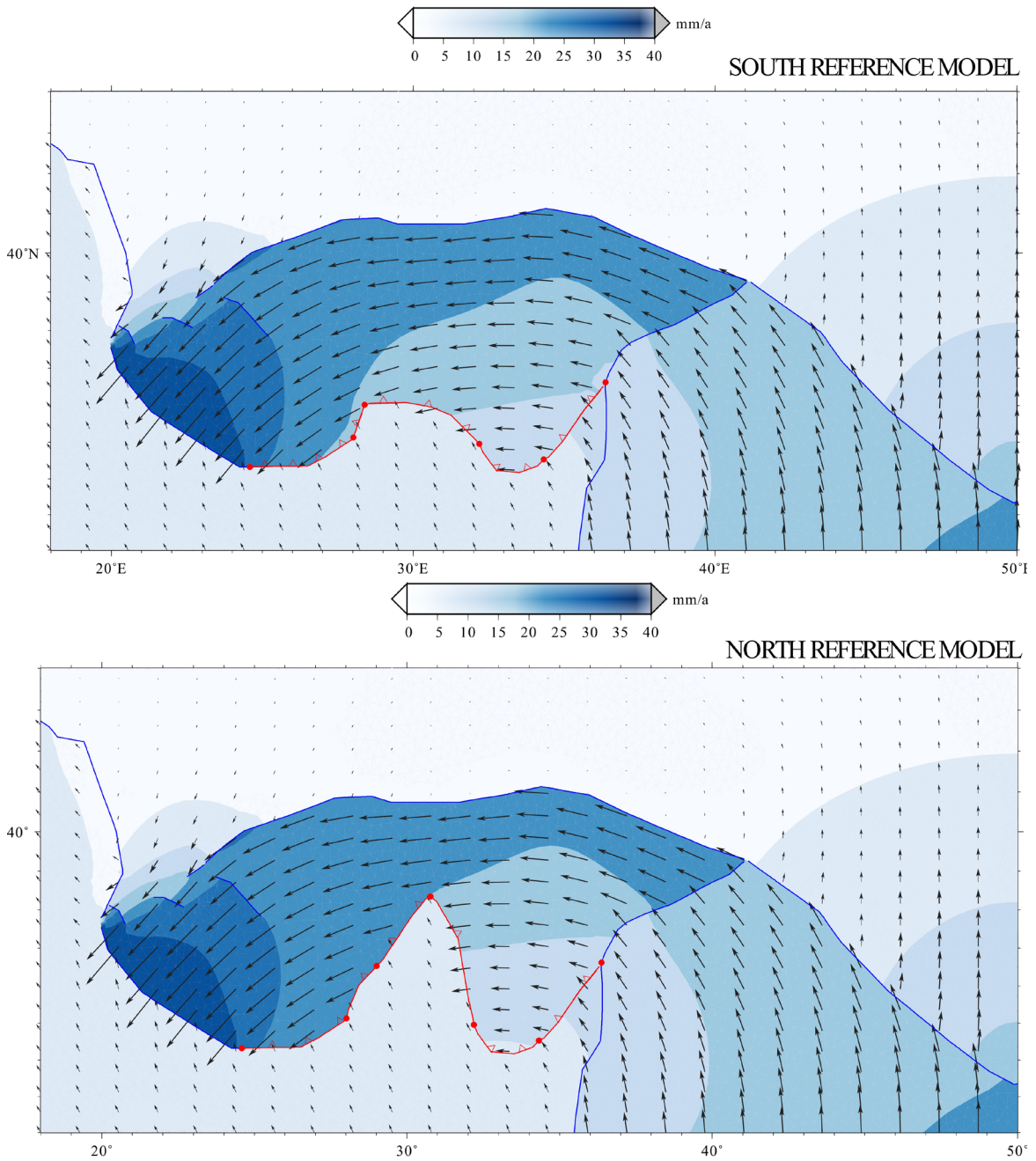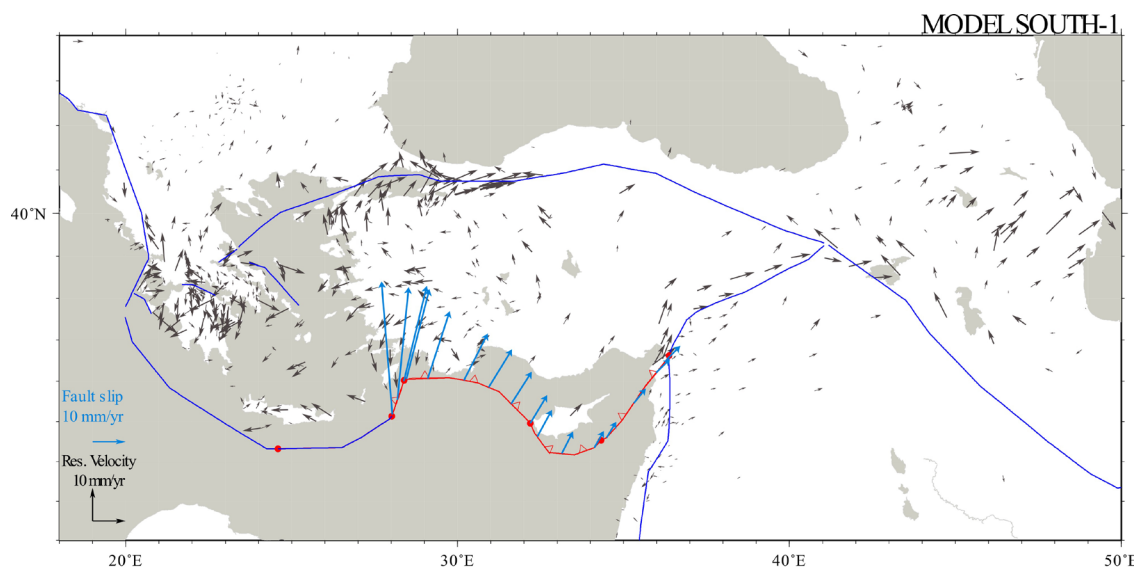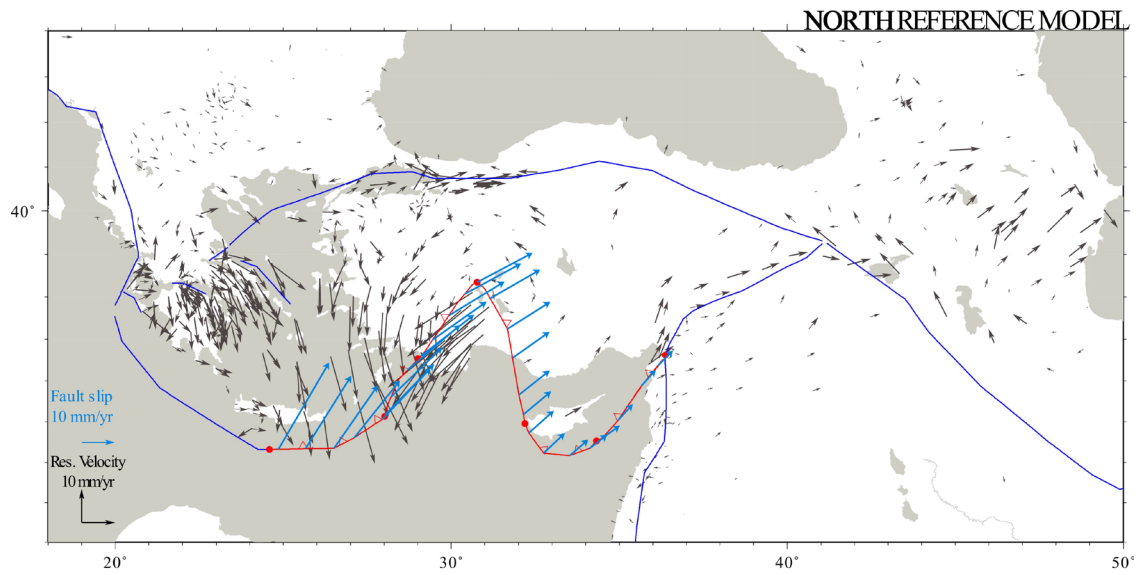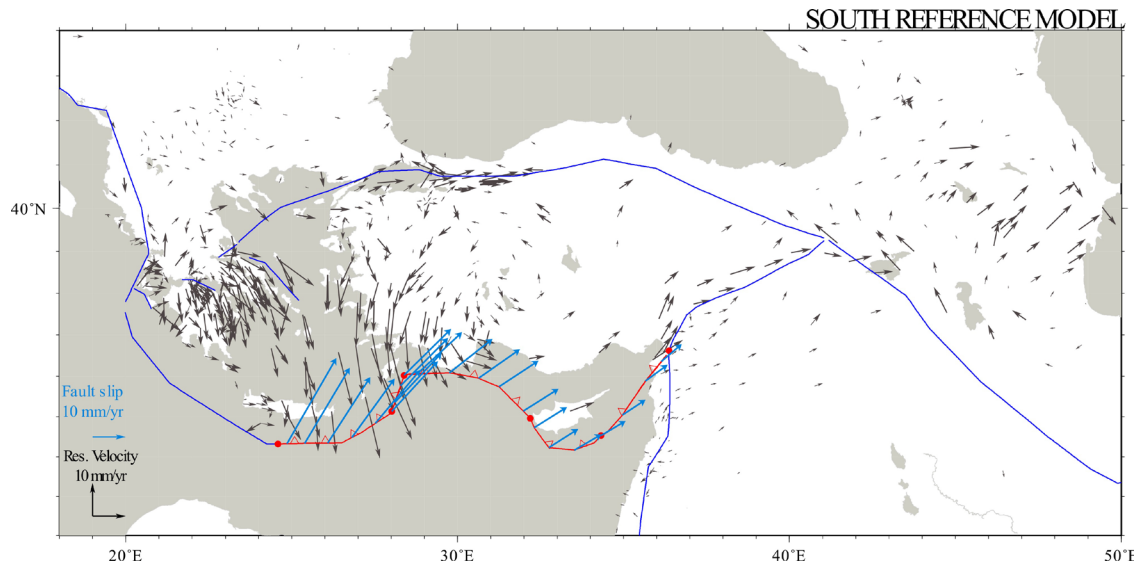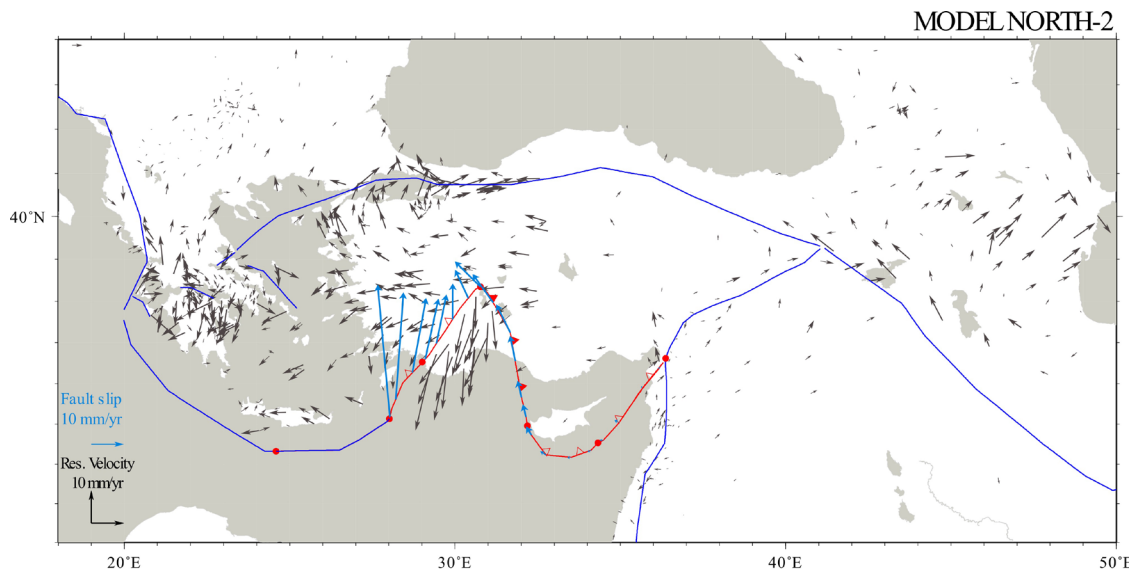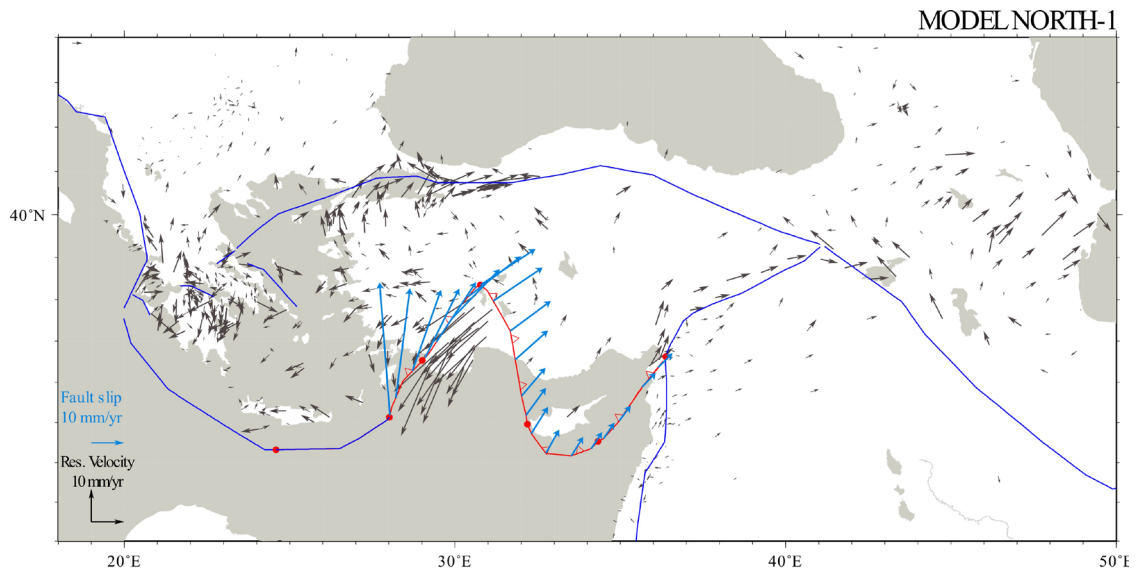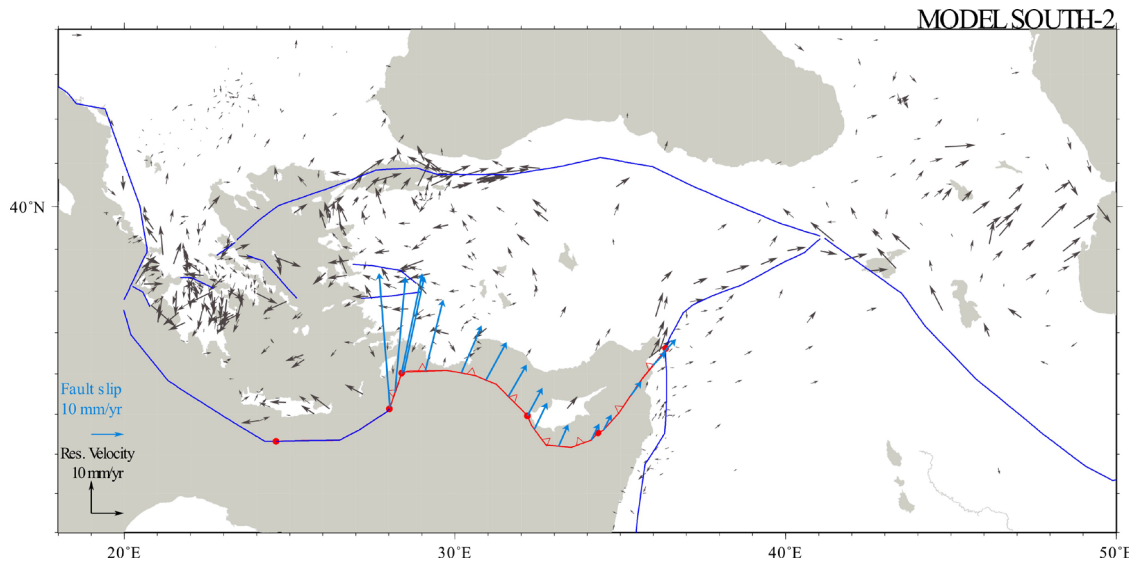
Figure 4. Model-predicted velocities and velocity misfits (observed minus calculated). The assumed nature of the faults is indicated by filled triangles when only fault-perpendicular motion is allowed and by strike-slip symbols when only fault parallel motion is allowed. Open triangles signify that both strike-slip and fault normal motions are allowed in the model. Blue arrows in the misfit maps (c–g) indicate the resulting fault slip-rate and direction. a) Velocities of the SOUTH reference model; b) velocities of the NORTH reference model; c) velocity misfits of the SOUTH reference model; d) velocity misfits of the NORTH reference model; e) velocity misfits of model SOUTH-1; f) velocity misfits of model SOUTH-2; g) velocity misfits for model NORTH-1; h) velocity misfits for model NORTH-2.

and the absence in the model of fundamental faults in the Caucasus and the Iranian Plateau. However, for our goal of identifying the plate boundary south of Anatolia these are unimportant details; model improvements would lead

to a better fit to the GPS observations in the east only. Vice versa, surface deformation in the easternmost part of the domain is practically the same for the NORTH and SOUTH scenarios, indicating that GPS velocities in the
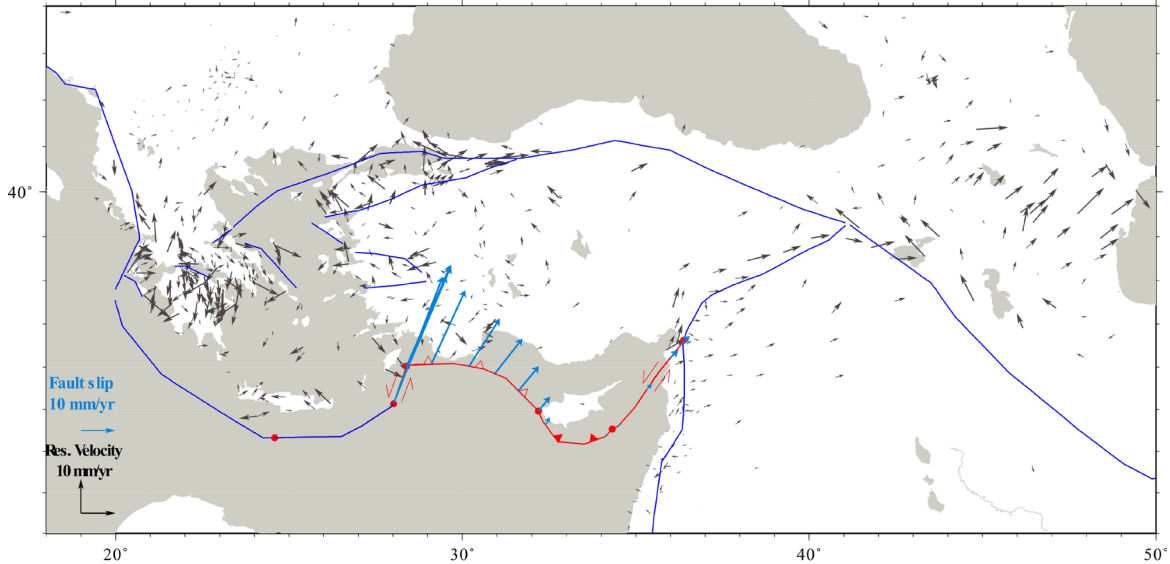
SOUTH REFERENCE MODEL

NORTH REFERENCE MODEL

MODEL SOUTH-1

MODEL SOUTH-2

MODEL NORTH-1

MODEL NORTH-2

MODEL SOUTH-6

Figure 5. Velocity misfits (observed minus calculated) for model SOUTH-6. Symbols show the assumed nature of the faults; filled triangles indicate that only fault-perpendicular motion is allowed, strike-slip symbols indicate that only fault parallel motion is allowed. Open triangles indicate that both strike-slip and fault normal motions are allowed in the model. Blue arrows indicate the resulting fault slip-rate and direction.

easternmost part of our domain are not sensitive to the details of the southern plate boundary of Anatolia. We will therefore not attempt to improve the model fit in the easternmost domain in the rest of this paper.

5.1.2. Models with additional forcing on the Pliny-Strabo segment

For both reference models, velocity misfits in western Anatolia and the southeastern Aegean region are large (Figures 4c and 4d). We therefore need to consider the need for additional drivers of surface deformation (e.g., forces related to the sinking of the Aegean slab, or gravitational collapse of the Aegean lithosphere). In the reference models we imposed the relative velocity along the Hellenic plate contact. In models SOUTH-1 and NORTH-1 we extend the forcing to include the Pliny-Strabo trenches by imposing the GPS-derived relative velocities here as well.

The results (Figures 4e and 4f) show that residual velocities have decreased in SE Anatolia and its surroundings. We therefore retain the extended forcing in subsequent models. We next investigate changes to the SOUTH and NORTH models individually in an attempt to further improve their fit with the GPS observations.

5.1.3. SOUTH plate boundary with additional Menderes faults

For the SOUTH plate boundary, the result in Figure 4e shows that the velocity residues are notably reduced in the Aegean Sea and western Turkey. However, near Rhodes and the SW edge of Turkey, misfits are still significant

and SSW and S directed. In the vicinity of the Menderes extensional province misfits are oriented E-W. To further improve upon this model we add another important geological element to the model: western Anatolia shows NNE directed extension and the Menderes massif horst-graben system takes up most of the deformation (Şengör, 1987). Thus, we add the Menderes faults as two parallel dip-slip faults to model SOUTH-2 corresponding to the Menderes and Gediz grabens, to loosen the coupling of NW Turkey from the SW. This modification yields smaller misfits (Figure 4f). Below we will seek to further improve the model fit by adding more faults, but the model SOUTH-2 already yields an acceptable fit to the observations in SE Turkey and surroundings.

5.1.4. NORTH plate boundary with friction

In the NORTH plate boundary configuration, the Isparta Angle moves with the Africa plate. Misfits in the Isparta Angle are significant in model NORTH-1 (Figure 4g). In model NORTH-2 we impose friction on the Aksu fault (E boundary of Isparta Angle) to allow westward push by Anatolia to penetrate into the Isparta Angle (Figure 4h). Irrespective of the frictional coupling we impose, the decrease in misfit is insufficient. Unless the Isparta Angle is detached from Africa, we cannot reproduce the GPS observations in the Isparta Angle. That is, there should exist another interface to the south of the Isparta Angle that accommodates the southwestward motion of the Isparta Angle.

5.1.5. Plate boundary configuration near southwest Anatolia

In the region closest to the NORTH and SOUTH plate boundaries, misfits for the NORTH model are significantly larger than for the SOUTH model. Geologically relevant possibilities for improvement of the NORTH model come to an end. We therefore conclude that the GPS velocities refute a NORTH plate boundary location. As the GPS observations are made onshore, this does not automatically prove our SOUTH plate boundary configuration to be correct. Below, we therefore seek to further improve the data fit of the SOUTH model to show that it at least is a very likely candidate for the plate boundary configuration.

5.2. SOUTH models: other regional faults

5.2.1. Adding friction on the Cyprus subduction contact: model SOUTH-3

The residual velocity of the Cyprus station is parallel to the direction of model slip vectors in model SOUTH-2 and its magnitude is similar to that of the slip vectors (Figure 4f). This residual velocity indicates that the Cyprus trench should have mechanical resistance to underthrusting –– thus far we assumed a frictionless interface. Stronger coupling is likely related to the collision of the ESM at the Cyprus trench (Ben-Avraham et al., 1988; Robertson, 1998; Mascle et al., 2000). In model SOUTH-3 (Appendix B, Figure B1a), we therefore seek to find the friction value that yields the minimum misfit at the Cyprus trench. In this model, we also restrict relative motion to be trench-perpendicular/down-dip only. The misfit at the Cyprus station and at Turkish stations along the coast facing Cyprus is within the limits of observational error when we select a shear stress of 3 MPa, equivalent to 42% coupling between opposite sides of the fault.

5.2.2. Varying the nature of the Rhodes fault: model SOUTH-4

The NNE striking fault bounding the Rhodes basin (RB in Figures 1 and 3) was thus far taken to accommodate both strike-slip and thrusting. In model SOUTH-4 we allow strike-slip only. The result (Figure B1b) shows an improved fit to the GPS velocity field. We conclude that this fault is strike-slip only.

5.2.3. Pure strike-slip Latakia segment: model SOUTH-5

Thus far, motion on the Latakia Fault segment could be both strike-slip and dip-slip, and it was found to be small and mostly strike-parallel. In model SOUTH-5, we only allow strike-slip to occur on the fault. The result (Figure B1c) shows that model velocities at nearby GPS stations are practically unaffected by this change (c.f. Figure B1b). Thus, although we cannot discriminate the two options based on the fit to the data, we prefer a strike-slip interpretation of the Latakia Fault as it is the simpler (fewer DOFs) model, but also because it agrees better with the seismotectonics of the region (Wdowinski et al., 2006).

5.2.4. Adding the south branch of the NAF in the west: model SOUTH-6

Inclusion of the southern branch of the NAF as a strike-slip fault into model SOUTH-6 leads to a decrease in chi-square norm from 7.75 to 7.55. The improvement of misfits can be seen in NE Turkey (Figure 5). Although, from a statistical point of view, the improvement is not very significant, the slip-rate predictions for the northern branch of the NAF give a better agreement with the geological slip-rate data if we include the southern branch. We will come back to this in Section 7.3 below.

5.2.5. Nature of the Burdur-Fethiye fault: models SOUTH-7 and SOUTH-8

With models SOUTH-7 and SOUTH-8 we investigate the imprint of the Burdur-Fethiye fault zone (BFFZ) on the surface velocity field. We implement the BFFZ as a strike-slip (one DOF) fault in both SOUTH-7 and SOUTH-8. In SOUTH-7, the BFFZ is disconnected from the plate boundary; in model SOUTH-8 it is connected to the Rhodes fault. Neither of the models (Figures B1d and B1e) results in slip on the BFFZ, so that the match to the GPS observations does not change. We conclude that the BFFZ is effectively locked or inactive at present.

Different from what we find, the block models of Tiryakioglu et al. (2013) and Reilinger et al. (2006) require a slip-rate on the BFFZ of up to 11 mm/year to reproduce the regional GPS observations. This illustrates a very important point: model results (including ours) are particularly sensitive to which faults to include or not, and whether the continuum between the faults is allowed to deform. As argued before, we think it is more realistic to add faults step-by-step to our deformation model and verify whether this results in a significant variance reduction. Crustal seismicity is too dispersed around the BFFZ to refute our conclusion that the fault is currently not active.

5.2.6. Independent Isparta block: model SOUTH-9

At this stage, testing the combination of the NORTH and SOUTH models, i.e. a model that contains the Isparta Angle crustal block, is the logical final step (SOUTH-9). The Isparta Block is bounded by the BFFZ and the Aksu faults. As such, the number of DOFs is the largest in the totality of the models. The misfit map (Figure 6) shows that the overall model agreement is more or less the same as in SOUTH-6 and the following models; however, the misfit statistics are slightly unfavorable. Most notable is the fact that inclusion of the Aksu fault does not significantly improve the velocity vectors in its vicinity. We therefore conclude that an independent Isparta block is a less viable option in view of the geodetic observations.

5.2.7. Significance of other regional faults

We further tested models with additional faults with regional significance that may affect the fit to the geodetic
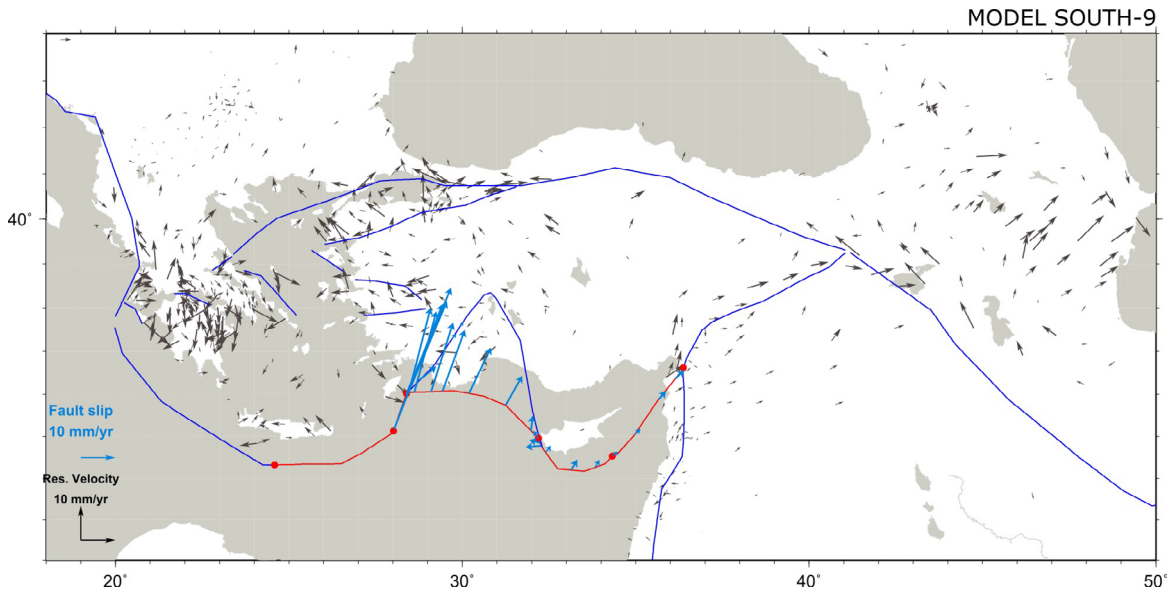
MODEL SOUTH-9

Figure 6. Velocity misfits (observed minus calculated) for model SOUTH-9, i.e. independent Isparta Block. The symbol explanations are the same as in Figure 5.

data, such as the Simav fault and Gökova faults. The slip-rate on these faults was found to be small and the corresponding improvement negligible. We therefore do not show these results.

5.2.8. Performance statistics of all models
In Appendix C, Figure C3 shows the X_R^2 statistic as a function of model number for GPS stations in the whole model domain (black circles) and for the box in Figure 1 (empty circles) — this is where the plate boundary configuration has the clearest impact. Model SOUTH-6 (Figure 5) is our "best" model from a statistical point of view, although it does not match observations within error in Greece and W Turkey, north of the EAF, and in the eastern part of the model. However, we refrain from trying to further improve this model fit by introducing smaller scale faults because the fit is acceptable near the SOUTH plate boundary. A notable exception is the Dodecanese, where additional, albeit minor, forces result in a more local change in velocity directions.

5.2.9. Conclusions
Model SOUTH-6 fits the GPS velocities best. We conclude that: (1) the plate boundary is located to the south of Anatolia. As part of this southern plate boundary (2) the prolongation of the Pliny-Strabo trenches to the NNE is strike-slip; (3) the ~W-E striking fault from the north of the Rhodes basin, to the Anaximander Mountains, to the W end of Cyprus, is predominantly a thrust contact; and (4) the Cyprus subduction contact is 42% locked. About other regional faults we conclude that: (5) the Burdur-Fethiye fault zone is locked or inactive, (5) the Menderes faults are active, and (6) the observations require the

southern strand of the North Anatolia Fault to be active.

5.3. Match of best fitting model SOUTH-6 to stress observations
WSM stress observations in our region of interest are largely based on focal mechanism data, i.e. they are as representative of the same (short) time scale as the geodetic data that we used to select model SOUTH-6. The stress concentrations shown in Figure 7 are the potential areas where intrablock seismic events can be expected. However, these stress concentrations are mainly controlled by geometry because we are not considering a single seismic cycle. That means the model cannot resolve intrablock seismicity in terms of loading history; it can only account for the secular deformation. It is noted that high stresses may result in distributed failure or flow. Such flow phenomena are not modeled in our approach. Here we test the extent to which the stress observations are consistent with the predictions of this model.

Figure 7 shows horizontal stress directions as predicted by the model and average directions of maximum compression from the WSM (Figure 2). The fit is remarkably good in Anatolia and Eurasia. Misfits are exclusively clustered along the Hellenic trench and around the Sea of Marmara. For the Hellenic trench, the model does not reproduce trench-normal compression in the accretionary wedge, most likely due to lack of fault friction in our model. It is interesting to note that in the model the Arabian plate interior and central Anatolia display low stress magnitudes; these regions are relatively aseismic. We conclude that available stress direction observations agree with the results of model SOUTH-6.
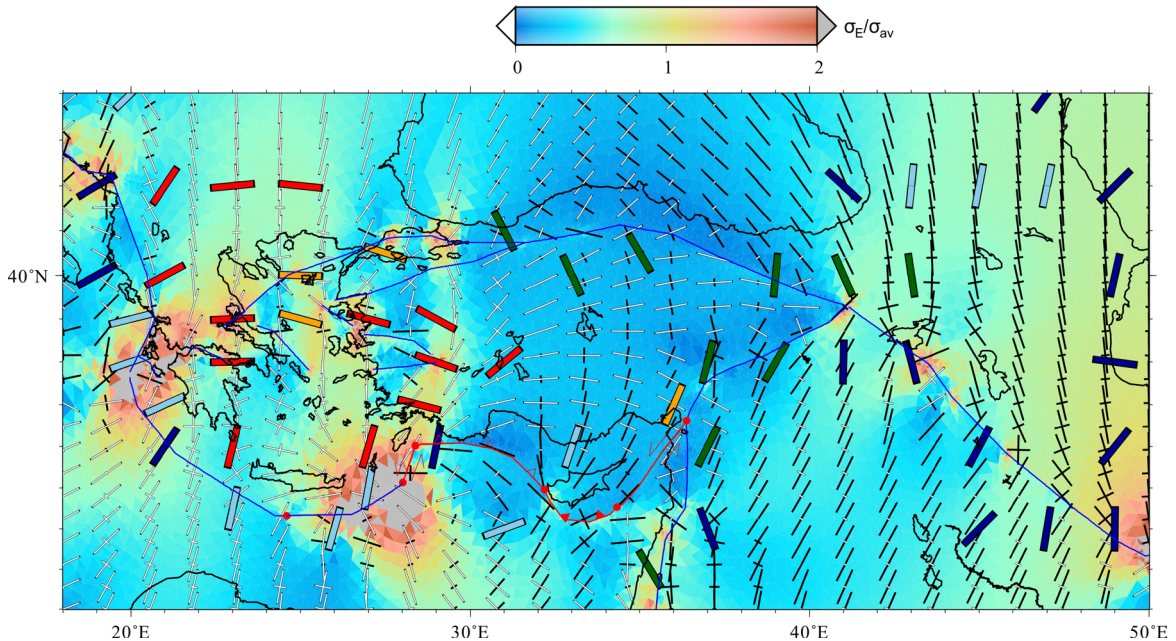
Figure 7. Stress field for model SOUTH-6. Black and white arrows indicate principal axis directions of horizontal compression and tension, respectively. Color contours indicate effective shear stresses (normalized by the average effective shear stress). Wide bars represent average WSM directions of maximum horizontal compression, with their color indicating the stress regime: dark blue for thrusting, light blue for oblique thrusting, green for strike-slip, orange for oblique tension, and red for tension (Figure 2).

5.4. Comparison of model slip-rates with geodetic modeling results from previous studies

Slip-rate is the rate of motion of the fault within a few or many earthquake cycles and thus reflects the short-term rates. Slip-rates can be determined from geodetic methods, such as GPS or InSAR (e.g., McClusky et al., 2000; Wright et al., 2004; Cavalie and Jonsson, 2104), but they always require a model: block-models, elastic or viscoelastic dislocation models, or combined fault/continuum models.

Figure 8 shows the compilation of previous slip-rate determinations with upper panel (Figure 8a) points to locations where these studies were conducted. The block model study of Meade et al. (2002) resulted in a slip-rate of 25.6 mm/year for the western NAF. Nyst and Thatcher (2004) found 24 mm/year for the Sea of Marmara region with their block model. The Reilinger et al. (2006) block model (Figure 8b, orange error bars showing the range of values on the y-axis and segment range on the x-axis) has an average of 27.5 mm/year to the west and 25 mm/year to the east of Düzce. McClusky et al. (2000) derived a constant value of 24 mm/year for the whole NAF from the GPS data (Figure 8b, brown dashed line). In the Sea of Marmara region, the difference between block models and our results (Figure 8b, banded graphs for model space and red line for best model SOUTH-6) exceeds ~5 mm/year. This discrepancy mainly results from the approach in block models to map geodetic velocities onto slip at

block boundaries, and to consider residues to result from continuum deformation (e.g., Nyst and Thatcher, 2004): this tends to maximize the fault slip-rate (fault potency rate) and explains why studies that make different choices regarding the partitioning of fault slip and continuum deformation (e.g., Provost et al., 2003; Flerit et al., 2004; Langstaff and Meade, 2013; this study) consistently find lower fault slip-rates.

As an alternative to block modeling, Flerit et al. (2004) utilized a fracture mechanics approach for the Anatolia deformation, where slip-rates for the NAF (Figure 7b, green error bars showing the range of values on the y-axis and segment range on the x-axis) agree with our results for slip-rate estimates in the Sea of Marmara region, but to the east they predict higher slip-rates. Thus, although in our study we do not constrain a priori where continuum deformation will be taking place as they do, differences appear to be too small to answer which of the methods is superior. Provost et al. (2003) applied far-field velocity conditions and the effect of the topography forcing in a 3D model with rheological complexities. Their slip-rate estimates (thick red error bars in Figure 8b, purple error bars representing point values) agree with our model results, albeit with much larger uncertainties.

Studies involving seismic moment tensor summation from earthquake catalogues also yield slip-rate estimates for the NAF (Figure 7b, light blue error bar at the right end of the
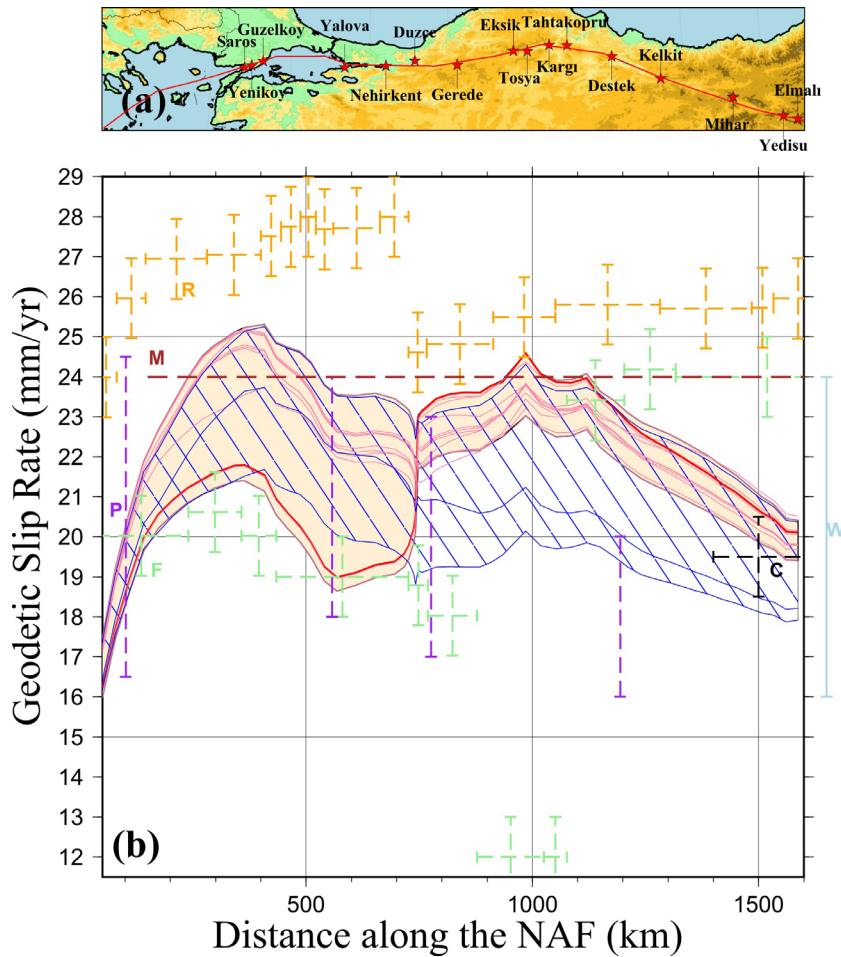
Figure 8. Comparison of present-day slip-rates on the North Anatolian Fault (NAF) zone with fault slip-rates from our models. a) Shaded relief map of the NAF region locations of geological slip-rate studies (red stars). b) Model slip-rates of SOUTH (orange shaded band) and NORTH (blue hachured band), with individual model slip-rate results shown by red and blue lines, respectively. Thick red line represents our best model (SOUTH-6). Model slip-rates are calculated for the northern branch of the NAF, whose geometry is given nearly parallel to the plot axis shown in panel (a). Brown colored line with label 'M' indicates the rate determined from the Eurasia-Anatolia Euler pole (McClusky et al., 2000). Discrete orange boxes with label 'R' represent the slip-rates from Reilinger et al. (2006) block model, where computation error is defined by the height of each box. Light green discrete lines with label 'F' represent Flerit et al.'s (2004) model slip-rates. Purple error bars with label 'P' indicate slip-rates determined from Provost et al. (2003). The seismic slip-rate estimates (Table 3, light blue bar at the right end of plot area) span a range of 16–24 mm/year for the NAF and represent the slip-rate value for the whole fault zone.

plot, indicating range of values: Jackson and McKenzie (1988), Kiratzi (1993), Westaway (1994), Ambraseys (2006)), agreeing well with our model results, partly because the range of seismic strain rates is very broad. In Appendix C (Figures C1 and C2) we compare modeled slip-rates with results from previous studies for the EAF and DSF. Our model slip-rates for both the EAF and DSF are lower than what previous studies showed, with the exception of seismic slip-rate results. Our results agree well with the range of seismic slip-rates. As explained in Section 5.1, we do not attempt to improve the model fit in the easternmost domain in

this paper; therefore, slip-rates within this part of the domain may be lower than what elastic block model studies indicate.

In conclusion, our slip-rate results for the NAF thus largely agree with previous work conducted in the region, with the exception of block-model estimates. Considering the 1 mm/year accuracy of the GPS-derived velocity data, variations in model slip-rates are large. This indicates that the overriding plate is sensitive to the southern boundary configuration, although this configuration's role is still subordinate to Hellenic trench and Arabian collisional boundary conditions.

6. "Geodetic" versus "geological" deformation

6.1. Context

Deformation after many earthquake cycles usually leaves an expression on the land surface, where the geomorphological features or sediments may be markedly displaced. Determination and dating of such offset markers or sediments yield the geologically determined slip-rates, although the definition of geological slip-rate is vague as long as the time span of "many earthquake cycles" is variable; usually a time interval of 1 to 1000 thousand years is implied (e.g., Tapponnier et al., 2001; Thatcher, 2009). Here we compare model slip-rates on the NAF and EAF with respect to geologically determined rates and, as such, discuss the validity of our model results on the scale of geological time. Furthermore, the agreement between geological and geodetic slip-rate is certainly important, because the difference between them is an indication of elastic strain accumulation, which may be released by earthquakes. We present results from the NAF here and leave the discussion for the DSF and EAF for Appendix C.

6.2. Slip-rate observations

Geological slip-rate observations represent average displacements divided by time from the early Pliocene-Quaternary until present. For the NAF the majority of the data average many seismic cycles and have a good coverage of the fault zone (Table 1 and black error bars in Figure 9). The geological slip-rate data have too sparse of a distribution to aid our analysis for the EAF (segments of the fault are indicated in Figure 10a). Therefore, we compiled published fault offsets (Table 2) and computed first-order estimates for the average slip-rate on the fault by dividing these offsets (Figure 10b) by the fault initiation time (2.9 Ma (Hubert-Ferrari et al., 2009) and 1.9 Ma (Herece, 2008)). Resultant slip-rates are shown in Figure 10c. This way of calculating slip-rates may underestimate the slip-rate values because faults usually evolve with time and fault segments do not accumulate displacements after the inception of the fault.

6.3. Comparison of data and models

In Figure 9, superimposed on all NORTH and SOUTH model bundles, geological slip-rates of NAF are shown with error bars (see Figure 8a for the location map). For the NAF, the best model, SOUTH-6 (thick red line), has a good fit to the data, except in the intervals of 700–900 km and 1000–1200 km. The model overall exhibits higher rates than the geological data. Previous model studies also found that geological rates were too low. The uncertainty in the data is so large that alternative configurations would have been possible. For example, whereas NORTH models show a better fit in the eastern part of the NAF (from 700 km onwards), SOUTH model fits are better in the west.

Overall our model results are within the error bars of geologically determined slip-rates along the NAF and we estimate an average slip-rate of 22 mm/year for the fault.

Figure 10d shows that model results for the EAF largely agree with the slip-rate data presented in Figure 10c, including the northernmost DSF, and if extrapolated further southwest, until Antakya (Seyrek et al., 2007) – the furthermost data point of Figure 10c lies outside of the panel. On the other hand, Çetin et al.'s (2003) paleoseismological slip-rates between Lake Hazar and Palu are underestimated by all models. The seismic slip-rate estimates (Table 3; Figure C1) span a range of 6–10 mm/year and agree with our slip-rate.

Figure 11 summarizes the correlation between average geological fault slip-rates and model results for major faults in our domain. Geological estimates predominantly reflect average slip-rates from the latest Pliocene-Quaternary until Present. Similar to Reilinger et al. (2006), we find good correlation between our model results and geological observations.

6.4. Vertical axis rotations

Vertical axis rotations are useful for comparison with paleomagnetic observations. Anatolia rotates counter-clockwise with variable rotation rates (Figure 12; Piper et al., 2010). Four data points on the Arabian plate show similar rotations coherent with Anatolia (van Dongen et al., 1967; Nur and Helsley, 1971). The Isparta Angle shows either no rotation or counter-clockwise rotations since the early Miocene (Meijers et al., 2011). Clockwise rotations in western and central Greece pervade to the Peloponnese (van Hinsbergen et al., 2005) and the westernmost Hellenic trench region. The eastern Hellenic trench displays counter-clockwise rotations, similar to Anatolia (Duermeijer et al., 2000).

Vertical axis rotations are computed for our preferred SOUTH-6 model, which is elastic. Hence, they are not finite rotations but indicate the potential for rotation to occur on geological time scales. We therefore only compare relative rotations. Our model results show good agreement with the sense of rotation of the data in central Anatolia and the Isparta Angle, mainland Greece, and the Hellenic trench region. Misfits are found in the northwest of Anatolia where the model produces counter-clockwise rotations, whereas data indicate the contrary. This may be due to the nonhomogeneous nature of rotations caused by the active tectonic movements. Furthermore, errors due to the nature of the paleomagnetic data (weak paleomagnetic signal, remagnetization, errors in age determination) result in a scatter of rotations. Overall, model rotations agree with the first-order features of the paleomagnetic data, although the data have large magnitude uncertainties.

Table 1. Compilation of geological slip-rate (slip-rate averaged over a few or more seismic cycles) determinations for the North Anatolian Fault. Ages of structures are reported in thousand years (ka). Numbers in the references column refer to: 1. Armijo et al., 1999; 2. Aksoy et al., 2010; 3. Meghraoui et al., 2012; 4. Schindler, 1997; 5. Polonia et al., 2004; 6. Dolan, 2009; 7. Dikbaş et al., 2009; 8. Pucci et al., 2008; 9. Kondo et al., 2010; 10. Kozacı et al., 2010; 11. Kozacı et al., 2009; 12. Hubert-Ferrari et al., 2002; 13. Zabci, 2012; Gray and white bands separate individual studies in the table.

Age (ka)	Slip-rate (mm/year)	Location	References
5000	14 ± 1[a]	Ganos segment	1
0.7 0.781 2.8 17.5 20.0	22.5 ± 0.5[b] 26.9 ± 0.6 17.0 ± 0.3 17.7 ± 18.9 17.9	Güzelköy Yeniköy Ganos segment	2
1	17 ± 5	Güzelköy	3
3000–4000	15–22	Sea of Marmara	4
10	10.0 ± 1.5[c]	Sea of Marmara	5
-	16–17	Sea of Marmara	6
1	21.9 ± 3.0	Nehirkent/Adapazarı	7
21.7 ± 1.9 60.1 ± 6.3 60	14.0 ± 2.1 15.2 ± 3.5 15.0 ± 3.2	Düzce	8
1	17–20	Gerede	9
2–2.5	20.5 ± 5.5 20.5 ± 8.5	Eksik	10
2–3	18.6 ± 3.4 16.4 + 6.4/-4.5	Tahtaköprü	11
10–12 10–12 10–12 10–12 1.64 ± 0.06	18.5 ± 3.5 18.5 ± 3.5 18.5 ± 3.5 18.5 ± 3.5 18 ± 5[d]	Eksik and Berçin Gerede Destek Mihar Üçoluk river/Tosya	12
2.5 ± 0.3 2.7 ± 0.5 3.3 ± 0.3 1.6 ± 0.1 1.3 ± 0.3 4.4 ± 0.5 1.6 + 0.1/-0.2	18.7 + 3.2/-2.8 19.9 + 4.2/-3.1 20.2 + 3.2/-2.8 17.7 + 5.4/-5.1 21.0 + 7.3/-4.6 18.8 + 4.0/-3.4 18.8 + 6.6/-6.0	Elmalı Yedisu Mihar Kelkit valley Kargı Tosya	13

[a]Stratigraphical age and the validity of the correlatable offset markers are disputed by Yaltırak et al. (2000) and Şengör et al (2005).
[b]This measurement was corrected and reinterpreted by Meghraoui et al. (2012), as listed below.
[c]Dolan (2009) discussed this measurement and reported a faster slip rate for the same location.
[d]According to Cowgill (2007) and Zabci (2012), the higher rate of 21 ± 2 reported by Hubert-Ferrari et al. (2002) is more reliable for this segment.

7. Discussion

7.1. Comparison with block models

Several studies inverted for a block model description of the GPS velocity field (Nyst and Thatcher, 2004; Reilinger et al., 2006; Floyd et al., 2010), whereas we treated the Anatolia–Aegean to be part of a deformation zone, allowing nonrigid behavior. The Anatolia–Aegean region exhibits varying deformation styles and we explain these complex deformation patterns with the least number of faults and blocks. Comparison of RMS error between
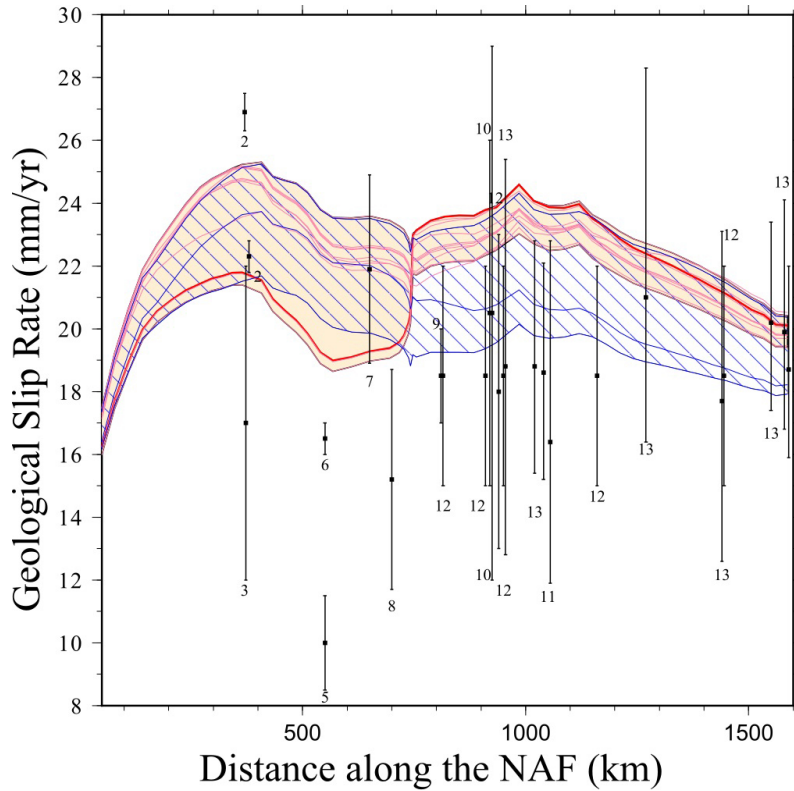
Figure 9. Comparison of geological slip-rates on the North Anatolian Fault (NAF) zone with fault slip-rates from our models. For location see shaded relief map in Figure 8a. Model slip-rates of SOUTH (orange shaded band) and NORTH (blue hachured band), with individual model slip-rate results shown by red and blue lines, respectively. Thick red line represents our best model (SOUTH-6). Model slip-rates are calculated for the northern branch of the NAF, whose geometry is given nearly parallel to the plot axis shown in Figure 8a. Observed slip-rates with error bars are labeled by numbers (Table 1).
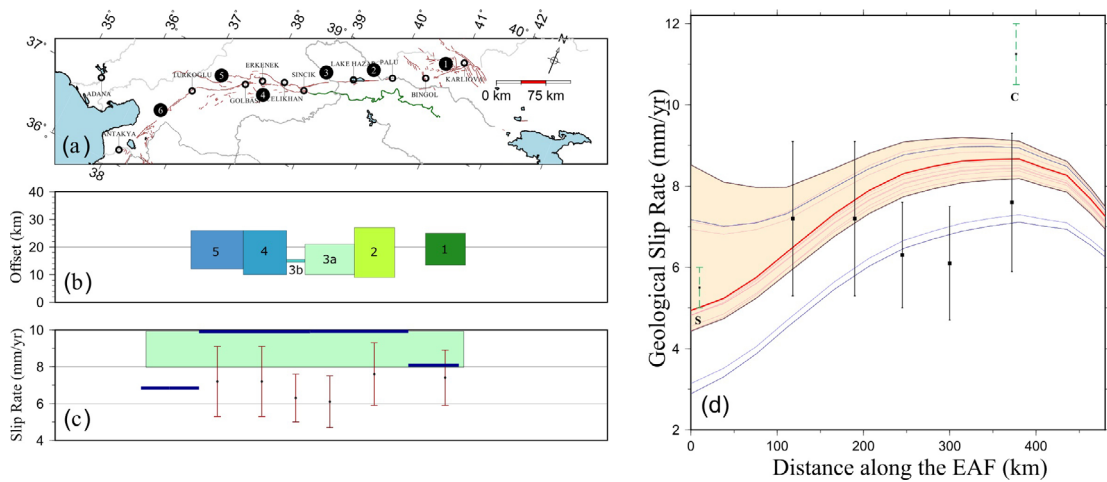

Figure 10. a) East Anatolian Fault from Karlıova to Antakya (Herece, 2008). Line segments in red show the EAF and green shows Bitlis suture zone. Major rivers in the region are shown in gray. Numbers indicate fault segments: 1. Karlıova - Bingöl, 2. Palu - Lake Hazar, 3. Sincik - Çelikhan , 4. Çelikhan - Gölbaşı, 5. Gölbaşı - Türkoğlu, 6. Türkoğlu - Antakya. b) Measured offsets on the fault, which are tabulated in Table 2. Boxes indicate the minimum and maximum estimates. c) Black points with error bars refer to slip-rates obtained from paleoseismology studies listed in Table 2. C: Çetin et al. (2003); S: Seyrek et al. (2007) and Karabacak et al. (2010). Red points with error bars are the long-term slip-rates of the EAF, calculated from Table 2. Light green box indicates the rate determined from the Eurasia-Anatolia Euler pole (McClusky et al., 2000). Discrete line segments are fault parallel slip-rates determined by mechanical models. Dark blue denotes Flerit et al. (2004), whereas Reilinger et al. (2006) slightly overlies the central segment of Flerit et al. (2004) for the whole EAF. Continuous red line with blue circles shows our slip-rate model results. d) Comparison of geological slip-rates on the East Anatolian Fault (EAF) zone with fault slip-rates from our models. For location see Figure 10(a). Model slip rates of SOUTH (orange shaded band) and NORTH (blue hachured band), with individual model slip rate results shown in red and blue lines, respectively. Thick red line represents our best model (SOUTH-6).

Table 2. Compilation of geological slip-rate (slip-rate averaged over a few or more seismic cycles) determinations for the East Anatolian Fault (EAF). The age of the fault is taken to be bracketed between 1.9 (Herece, 2008) and 2.9 Ma (Hubert-Ferrari at al., 2009). Ages of structures are reported in million years (Ma). Slip-rates are determined by dividing the measured offsets into fault age (1.9–2.9 Ma). Numbers in the references column refer to: 1. Herece, 2008; 2. Seymen and Aydın, 1972; 3. Dewy et al., 1986; 4. Şaroğlu et al., 1992; 5. Hubert-Ferrari et al., 2009; 6. Arpat and Şaroğlu, 1972; 7. Herece and Akay, 1992; 8. Turan, 1993; 9. Çetin et al., 2003; 10. Arpat and Şaroğlu, 1975; 11. Hempton, 1985; 12. Şaroğlu et al., 1987; 13. Parlak, 2004; 14. Westaway and Arger, 1996; 15. Yönlü et al., 2012; 16. Seyrek et al., 2007; 17. Karabacak et al., 2010. Gray and white bands separate each segment of the EAF system. Numbers in parentheses in the location column are used in Figure 10.

Age (Ma)	Offset (km)	Slip-rate (mm/year)	Location	References
1.9	14.5 ± 1	6.0 ± 1.7	Karlıova – Bingöl (1)	1
	15	6.3 ± 1.3		2
	22	9.2 ± 1.9		3
2.88	20 ± 5	8.3 ± 3.8		4 and 5
1.9	16 ± 1	6.7 ± 1.8	Palu – Lake Hazar (2)	1
1.9	15–23	7.9 ± 3.3		2
	27[a]	11.3 ± 2.3		6
	9	3.8 ± 0.8		7
	11	4.6 ± 0.9		8
0.014–0.015	0.16–0.175	11 ± 0.9		9
	16	6.7 ± 1.4	Hazar – Sincik (3a)	1
	10	4.2 ± 0.9		7
1.9	15	6.3 ± 1.3		10
	21 (17)[b]	7.9 ± 2.5		11
	13[c]	5.4 ± 1.1		12
	15	6.3 ± 1.3	Sincik – Çelikhan (3b)	6
1.9	22.5–26[d]	10.1 ± 2.8	Çelikhan – Gölbaşı (4)	1
		4.2 ± 0.9		13
1.9	19–25	9.2 ± 3.2	Gölbaşı – Türkoğlu (5)	1
1.9	22.5–26.0[e]	10.1 ± 2.8		1
1.9	12	5.0 ± 1.0		1
	13[f]	5.4 ± 1.1		4
1.9	16	6.7 ± 1.4		14
	16.5 ± 1.0	6.9 ± 1.8		15
			Türkoğlu – Antakya (6)	
		5.6 ± 0.5	Northernmost Dead Sea Fault	16
	7.9 ± 0.3	4.9 ± 0.1		17

[a]Cited by Cetin et al. (2003).

[b]Westaway and Arger (1996) measured 17 km of offset from Hempton's (1985) map.

[c]Cited by Parlak (2004).

[d]Near Erkenek.

[e]Near Gölbaşı.

[f]Göksu River offset cited by Westaway and Arger (1996).

previous block models and our study is shown in Table 4. Our RMS error magnitudes are very similar to the errors of block model studies.

Reilinger et al. (2006) argued from their kinematic study that the westward motion and counter-clockwise rotation of Anatolia do not comply with the extrusion process, while the increasing velocities of Anatolia towards the Hellenic trench suggest that slab rollback and accompanying overriding plate motion is a better dynamic explanation. Our model results are at odds with

their conclusion. The combined effect of the Arabian push and Hellenic trench pull constitutes the main driving boundary conditions for this deformation zone, as shown by Meijer and Wortel (1996, 1997), and justified by our own model. Furthermore, Reilinger et al. (2006) identified a mismatch between geological and GPS-derived slip-rates for the NAF. The authors attributed the difference to geological surface offsets that do not reflect the full rate at depth due to off-fault shallow deformation. This is a likely explanation. Another contribution to differences between

Table 3. Slip-rate estimates from moment tensor summation. Numbers in the references column refer to: 1. Jackson and McKenzie, 1988; 2. Kiratzi, 1993; 3. Westaway, 1994; 4. Ambraseys, 2006; 5. Kuran, 1980. Gray and white bands separate the estimates of NAF from EAF system.

Time frame	Slip-rate (mm/year)	Notes	Location	Study
1900–1988	25–30		NAF	1
1850–1988	23		NAF	2
1900–1992	30		30°E–40°E	3
1900–1992	8	Ignoring 1939–1967 seismicity and the background seismicity		
1668–1967	14.7	Ignoring 1939–1967 seismicity		
1668–1967	16.8	Including Marmara	26°E–40°E	
1668–1967	15–17	Most likely rates	26°E–40°E	
0–2000	20 ± 4		26°E–31°E	4
1850–1988	6		EAF	1
	4.4		EAF	2
1500–1988	6		EAF	3
995–1980	10		EAF	5

Figure 11. Spatially averaged geological slip rates vs. slip rates of best model SOUTH-6 for the Dead Sea Fault (DSF), East Anatolian Fault (EAF), Zagros Main Recent Fault (MRF), and North Anatolian Fault (NAF).

geological and geodetic slip-rates may result from their block approach, which is based on rigid blocks. Hergert and Heidbach (2010) showed that a more appropriate model, which allows internal deformation, accounts for slip-rates in the Marmara segment of the NAF, which are considerably smaller than the block model results and also compatible with the geological rates. In our approach we generalized this finding to the whole of the NAF. We find that the slip-rate estimates are within the error margins of geologically derived slip-rate data.
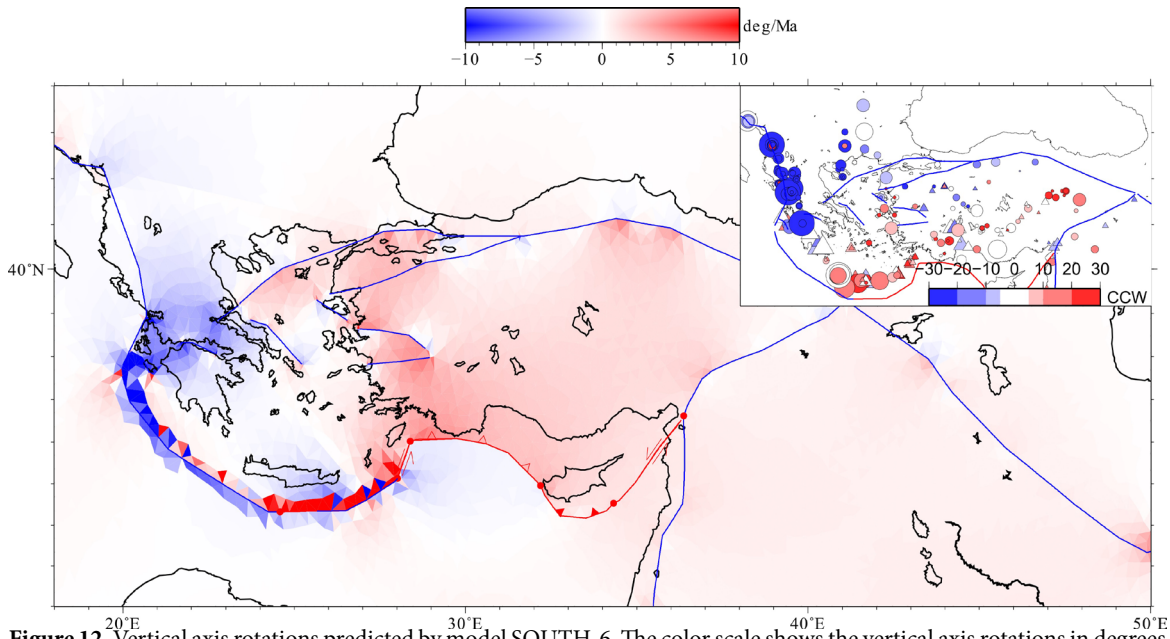
Figure 12. Vertical axis rotations predicted by model SOUTH-6. The color scale shows the vertical axis rotations in degrees per Myr. Blue and red colors indicate clockwise and counter-clockwise motions, respectively. Inset: Paleomagnetic rotation data (see the main text for references). Circles show pre-Pliocene sampling sites and triangles represent Oligocene and Miocene sample sites. Diameter of symbols are scaled with α_{95} value (larger symbol indicates a more reliable measurement).

Table 4. Comparison of RMS error between previous block models and this study.

Study	Number of blocks	RMS (mm/year)
Nyst and Thatcher (2004)	4	3.9
Reilinger et al. (2006)	6	3.9
Floyd et al. (2010)	10	2.8
	15	2.6
This study	-	4.1

African and Arabian motion from plate tectonic estimates differed insignificantly from the GPS rate for the past 11 and 22 Myrs, respectively (ArRajehi et al., 2010), although, prior to the Pliocene, active deformation of Anatolia was influenced by different fault geometries. Moreover, the relative motion at the Hellenic trench might have been different (Meijer and Wortel, 1996; Royden and Papanikolau, 2011). The agreement of our slip-rate model results and the geological data indicates that the mechanical model describes the deformation of this region from the early Pleistocene onwards. Unfortunately, the slip-rate data do not constrain the effect of a variation in the relative plate motion on the Hellenic trench and fault geometries. Using primarily the Aegean dataset Reilinger et al. (2010) arrived at the same conclusion concerning the coherence of geological and present-day deformation rates. Our results improve their findings, especially for the NAF and EAF slip-rate estimates.

7.2. How long has the present-day plate boundary configuration existed?

We consider fault slip-rates as important recorders of changes in the plate boundary configuration. Geological slip-rate data on major regional faults span a variety of ages, from several million years to tens of thousands and even a few hundred years. The compatibility of model results with slip-rates (Figure 11) obtained from such a large age spectrum is intriguing. Geological slip-rates are sensitive to two factors: the geometry of the faults and the far-field (plate tectonic) velocities, and both have varied in the recent geological past. First, the NAF is a relatively young feature. The NAF entered the Sea of Marmara at around 200 ka (Le Pichon et al., 2001), implying that the whole strike-slip system acquired its overall geometry after 200 ka. However, deformation related to the NAF predecessor (the wider North Anatolian Shear Zone from which the NAF localized) was evident in the Sea of Marmara since

the late Miocene (Şengör et al., 2005). In fact, prior to 200 ka, the NAF had accumulated more than 90% of its total offset (Şengör et al., 2005) here. Thus, the geometry of the NAF used in this study has been more or less mature for the comparison between the geological and model (geodetic) time scale to be valid. For the EAF, after the initiation of the EAF at around 2.9 (Hubert-Ferrari et al., 2009) or 1.9 Ma (Herece, 2008), the geometry of major faults in the east did not change much.

Geological slip-rates are also sensitive to the plate tectonic velocities and changes therein. According to ArRajehi et al., (2010) the present-day Arabia motion with respect to Eurasia obtained from GPS and plate tectonic estimates since the Miocene are consistent within uncertainties. The migration rate of the Hellenic trench has increased since the Oligocene (Royden and Papanikolaou, 2011; van Hinsbergen and Schmid, 2012), with significant lateral variations from west to east. Slip-rates along the NAF increased also since the middle Miocene (Hubert-Ferrari et al., 2002). The nature and location of the southern plate boundary may thus have existed since a few Myrs, and possibly longer.

8. Conclusions
Observations of near-surface deformation in and near the Anatolian-Aegean region agree best with an Aegean–Anatolian southern plate boundary via the Pliny-Strabo trench - Anaximander Mountains - ESM collision south of the Cyprus - Latakia ridge. The sense of motion along this boundary is defined by (1) an Anaximander Mountains fault with both strike-slip and dip-slip components and (2) predominant strike-slip along the Latakia segment. The southern plate boundary as preferred for the present day (SOUTH configuration) may have existed since the Late Pliocene.

In addition to well-established faults in Anatolia, the surface deformation requires an inactive Burdur–Fethiye fault zone, active Menderes faults, and an active southern strand of the NAF in NW Turkey

References

Aksoy ME, Meghraoui M, Cakir Z, Ferry M, Uçarkuş G (2010). Short-term and long-term slip rate along the westernmost segment of the North Anatolian Fault using paleoseismic trenching and drainage offsets. In: EGU General Assembly Conference Abstracts 12: 12447.

Aksu A, Hall J, Yaltırak C (2009). Miocene–Recent evolution of Anaximander Mountains and Finike Basin at the junction of Hellenic and Cyprus Arcs, eastern Mediterranean. Mar Geol 258: 24-47.

Aksu AE, Calon T, Hall J, Mansfield S, Yasar D (2005). The Cilicia–Adana basin complex, eastern Mediterranean: Neogene evolution of an active fore-arc basin in an obliquely convergent margin. Mar Geol 221: 121-159.

Aktuğ B, Nocquet JM, Cingoz A, Parsons B, Erkan Y, England P, Lenk O, Gurdal MA, Kılıçoğlu A, Akdeniz H et al. (2009). Deformation of western Turkey from a combination of permanent and campaign GPS data: limits to block-like behavior. J Geophys Res 114: B10404.

Alchalbi A, Daoud M, Gomez F, McClusky S, Reilinger R, Romeyeh MA, Alsouod A, Yassminh R, Ballani B, Darawcheh R et al. (2010). Crustal deformation in northwestern Arabia from GPS measurements in Syria: slow slip rate along the northern Dead Sea Fault. Geophys J Int 180: 125-135.

Alçiçek M, Veen JT, Özkul M (2006). Neotectonic development of the Çameli Basin, south-western Anatolia, Turkey. Geol Soc Spec Publ 260: 591-611.

Allen M, Jackson J, Walker R (2004). Late Cenozoic reorganization of the Arabia-Eurasia collision and the comparison of short-term and long-term deformation rates. Tectonics 23: TC2008.

Ambraseys NN (2006). Comparison of frequency of occurrence of earthquakes with slip rates from long-term seismicity data: the cases of Gulf of Corinth, Sea of Marmara and Dead Sea Fault Zone. Geophys J Int 165: 516-526.

Armijo R, Meyer B, Hubert A, Barka A (1999). Westward propagation of the North Anatolian fault into the northern Aegean: timing and kinematics. Geology 27: 267-270.

Arpat E, Şaroğlu F (1972). The East Anatolian fault system: thoughts on its development. Bulletin of the Mineral Research and Exploration Institute of Turkey 78: 33-39.

Arpat E, Şaroğlu F (1975). Türkiye'deki bazı önemli genç tektonik olaylar. Bulletin of the Geological Society of Turkey 18: 29-41 (in Turkish).

ArRajehi A, McClusky S, Reilinger R, Daoud M, Alchalbi A, Ergintav S, Gomez F, Sholan J, Bou-Rabee F, Ogubazghi G et al (2010). Geodetic constraints on present-day motion of the Arabian plate: implications for Red Sea and Gulf of Aden rifting. Tectonics 29: TC3011.

Baes M, Govers R, Wortel MJR (2011). Subduction initiation along the inherited weakness zone at the edge of a slab: insights from numerical models. Geophys J Int 184: 991-1008.

Baker C, Hatzfeld D, Lyon-Caen H, Papadimitriou E, Rigo A (1997). Earthquake mechanisms of the Adriatic sea and western Greece: implications for the oceanic subduction-continental collision transition. Geophys J Int 131: 559-594.

Barka A, Reilinger R (1997). Active tectonics of the Eastern Mediterranean region: deduced from GPS, neotectonic and seismicity data. Ann Geophys 40: 587-611.

Bassin C, Laske G, Masters, G (2000). The current limits of resolution for surface wave tomography in North America. EOS T Am Geophys Un 81: F897.

Ben-Avraham Z, Kempler D, Ginzburg A (1988). Plate convergence in the Cyprian Arc. Tectonophysics 146: 231-240.

Bijwaard H, Spakman W (2000). Non-linear global P-wave tomography by iterated linearized inversion. Geophys J Int 141: 71-82.

Biryol C, Beck S, Zandt G, Özacar A (2011). Segmented African lithosphere beneath the Anatolian region inferred from teleseismic P-wave tomography. Geophys J Int 184: 1037-1057.

Boray A, Şaroğlu F, Emre Ö (1985). Isparta büklümünün kuzey kesiminde doğu-batı daralma için bazı veriler. Jeoloji Mühendisliği 23: 9-20 (in Turkish).

Bozkurt E (2001). Neotectonics of Turkey – a synthesis. Geodin Acta 14: 3-30.

Burchfiel BC, King RW, Todosov A, Kotzev V, Durmurdzanov NTS, Nurce B (2006). GPS results for Macedonia and its importance for the tectonics of the Southern Balkan extensional regime. Tectonophysics 413: 239-248.

Calon T, Aksu A, Hall J (2005). The Neogene evolution of the outer Latakia basin and its extension into the eastern Mesaoria basin (Cyprus), eastern Mediterranean. Mar Geol 221: 61-94.

Carminati E, Wortel MJR, Meijer P, Sabadini R (1998). The two-stage opening of the western central Mediterranean basins: a forward modeling test to a new evolutionary model. Earth Planet Sc Lett 160: 667-679.

Cavalie O, Jonsson J (2014). Block-like plate movements in eastern Anatolia observed by InSAR. Geophys Res Lett 41: 26-31.

Çetin H, Güneyli H, Mayer L (2003). Paleoseismology of the Palu-Lake Hazar segment of the east Anatolian fault zone, Turkey. Tectonophysics 374: 163-197.

Cianetti S, Gasperini P, Giunchi C, Boschi E (2001). Numerical modelling of the Aegean-Anatolian region: geodynamical constraints from observed rheological heterogeneities. Geophys J Int 146: 760-780.

Cowgill E (2007). Impact of riser reconstructions on estimation of secular variation of strike-slip faulting: revisiting the Cherchen river site along the Altyn Tagh fault, NW China. Earth Planet Sc Lett 254: 239-255.

Dewey J, Şengör AMC (1979). Aegean and surrounding regions: Complex multiplate and continuum tectonics in a convergent zone. Geol Soc Am Bull 90: 84-92.

Dewey JF, Hempton MR, Kidd WSF, Şaroğlu F, Şengör AMC (1986). Shortening of continental lithosphere: the neotectonics of Eastern Anatolia – a young collision zone. Geol Soc Spec Publ 19: 1-36.

Dikbaş A, Akyüz HS, Meghraoui M, Ferry M, Yalçıner CC, Zabcı C, Karabacak V, Kiyak N, Altunel E (2009). Earthquake history and slip rate of Sapanca - Akyazı segment on western part of North Anatolian Fault for the past 1000 years. In: 62nd Geological Congress of Turkey, Abstracts, p. 1001.

Dolan J (2009). Possible transient strain accumulation along the north Anatolian fault (NAF): Precursor or artifact? In: Seismological Society of America "1509 Marmara Earthquake" Symposium, İstanbul, pp. 80-82.

Duermeijer C, Nyst M, Meijer P, Langereis C, Spakman W (2000). Neogene evolution of the Aegean arc: paleomagnetic and geodetic evidence for a rapid and young rotation phase. Earth Planet Sc Lett 176: 509-526.

Emre Ö, Duman TY, Özalp S, Elmacı H, Olgun Ş, Şaroğlu F (2013). Active Fault Map of Turkey with an Explanatory Text. Ankara, Turkey: General Directorate of Mineral Research and Exploration, Special Publication Series-30.

England P, McKenzie D (1982). A thin viscous sheet model for continental deformation. Geophys J Roy Astr S 70: 295-321.

Eyidoğan H, Barka A (1996). The 1 October 1995 Dinar earthquake, SW Turkey. Terra Nova 8: 479-485.

Faccenna C, Bellier O, Martinod J, Piromallo C, Regard V (2006). Slab detachment beneath eastern Anatolia: a possible cause for the formation of the North Anatolian fault. Earth Planet Sc Lett 242: 85-97.

Fischer KD (2006). The influence of different rheological parameters on the surface deformation and stress field of the Aegean-Anatolian region. Int J Earth Sci 95: 239-249.

Flerit F, Armijo R, King G, Meyer B (2004). The mechanical interaction between the propagating North Anatolian Fault and the back-arc extension in the Aegean. Earth Planet Sc Lett 224: 347-362.

Floyd M, Billiris H, Paradissis D, Veis G, Avallone A, Briole P, McClusky S, Nocquet J, Palamartchouk K, Parsons B et al. (2010). A new velocity field for Greece: implications for the kinematics and dynamics of the Aegean. J Geophys Res 115: B10403.

Ghosh A, Holt WE, Flesch LM (2009). Contribution of gravitational potential energy differences to the global stress field. Geophys J Int 179: 787-812.

Got JL, Monteiller V, Monteux J, Hassani R, Okubo P (2008). Deformation and rupture of the oceanic crust may control growth of Hawaiian volcanoes. Nature 451: 453-456.

Govers R, Meijer P (2001). On the dynamics of the Juan de Fuca plate. Earth Planet Sc Lett 189: 115-131.

Govers R, Wortel MJR (2005). Lithosphere tearing at STEP faults: response to edges of subduction zones. Earth Planet Sc Lett 236: 505-523.

Grad, M, Tiira T, ESC Working Group (2009). The Moho depth map of the European Plate. Geophys J Int 176: 279-292.

Hall J, Aksu A, Elitez İ, Yaltırak C, Çiftçi G (2014). The Fethiye-Burdur Fault Zone: a component of upper plate extension of the subduction transform edge propagator fault linking Hellenic and Cyprus arcs, eastern Mediterranean. Tectonophysics 635: 80-99.

Hall J, Aksu AE, Yaltırak C, Winsor JD (2009). Structural architecture of the Rhodes basin: a deep depocentre that evolved since the Pliocene at the junction of Hellenic and Cyprus arcs, eastern Mediterranean. Mar Geol 258: 1-23.

Heidbach O, Tingay M, Barth A, Reinecker J, Kurfess D, Müller B (2008). The World Stress Map Database Release 2008. Paris, France: Commission for the Geological Map of the World.

Heidbach O, Tingay M, Barth A, Reinecker J, Kurfess D, Müller B (2010). Global crustal stress pattern based on the World Stress Map database release 2008. Tectonophysics 482: 3-15.

Hempton MR (1985). Structure and deformation history of the Bitlis suture near lake Hazar, south-eastern Turkey. Bull Geol Soc Am 96: 233-243.

Herece E (2008). Doğu Anadolu fay (DAF) Atlası. Özel yayın serisi. Ankara, Turkey: Maden Tetkik Arama Genel Müdürlüğü (in Turkish).

Herece E, Akay E (1992). Karlıova - Çelikhan arasında Doğu Anadolu Fayı. In: Türkiye 9. Petrol Kongresi. Ankara, Turkey: TMMOB Petrol Mühendisleri Odası, pp. 361-362 (in Turkish).

Hergert T, Heidbach O (2010). Slip-rate variability and distributed deformation in the Marmara Sea fault system. Nat Geosci 3: 132-135.

Hessami K, Nilforoushan F, Talbot CJ (2006). Active deformation within the Zagros Mountains deduced from GPS measurements. J Geol Soc London 163: 143-148.

Hollenstein C, Müller M, Geiger A, Kahle HG (2008). Crustal motion and deformation in Greece from a decade of GPS measurements, 1993–2003. Tectonophysics 449: 17-40.

Hubert-Ferrari A, Armijo R, King G, Meyer B, Barka A (2002). Morphology, displacement, and slip rates along the North Anatolian Fault, Turkey. J Geophys Res 107: ETG 9-1-ETG 9-33.

Hubert-Ferrari A, King G, Woerd J, Villa I, Altunel E, Armijo R (2009). Long-term evolution of the North Anatolian Fault: new constraints from its eastern termination. Geol Soc Spec Publ 311: 133-154.

Jackson J, McKenzie D (1998). The relationship between plate motions and seismic moment tensors, and rates of active deformation in the Mediterranean and Middle East. Geophys J Int 93: 45-73.

Jimenez-Munt I, Sabadini R (2002). The block-like behavior of Anatolia envisaged in the modeled and geodetic strain rates. Geophys Res Lett 29: 39/1-39/4.

Jimenez-Munt I, Sabadini R, Gardi A, Bianco G (2003). Active deformation in the Mediterranean from Gibraltar to Anatolia inferred from numerical modeling and geodetic and seismological data. J Geophys Res 108: ETG 2-1-ETG 2-24.

Karabacak V, Altunel E, Meghraoui M, Akyüz H (2010). Field evidences from northern Dead Sea Fault Zone (South Turkey): new findings for the initiation age and slip rate. Tectonophysics 480: 172-182.

Keskin M (2003). Magma generation by slab steepening and breakoff beneath a subduction-accretion complex: an alternative model for collision-related volcanism in Eastern Anatolia, Turkey. Geophys Res Lett 30: GL018019.

Ketin İ (1948). Über die tektonisch-mechanischen Folgerungen aus den grossen anatolischen Erdbeben des letzten Dezenniums. Geol Rundsch 36: 77-83 (in German).

Kiratzi AA (1993). A study on the active crustal deformation of the North and East Anatolian fault zones. Tectonophysics 225: 191-203.

Kiratzi AA, Papazachos CB (1995). Active crustal deformation from the Azores triple junction to the Middle East. Tectonophysics 243: 1-24.

Kotzev V, Nakov R, Georgiev T, Burchfiel BC, King RW (2006). Crustal motion and strain accumulation in western Bulgaria. Tectonophysics 413: 127-145.

Kozacı Ö, Dolan J, Finkel R, Hartleb R (2007). Late Holocene slip rate for the North Anatolian Fault, Turkey, from cosmogenic 36Cl geochronology: implications for the constancy of fault loading and strain release rates. Geology 35: 867-870.

Kozacı Ö, Dolan JF, Finkel R (2009). A late Holocene slip rate for the central North Anatolian fault, at Tahtaköprü, Turkey, from cosmogenic 10Be geochronology: Implications for fault loading and strain release rates. J Geophys Res 114: B01405.

Kreemer C, Holt W, Haines A (2003). An integrated global model of present-day plate motions and plate boundary deformation. Geophys J Int 154: 8-34.

Kuran U (1980). The location magnitude and long-term time prediction of damaging earthquake along Anatolian faults and Levant coast. In: Bulletin of the Geophysical Congress of Turkey 2, pp. 151-163.

Le Pichon X, Şengör AMC, Demirbağ E, Rangin C, Imren C, Armijo R, Görür N, Çağatay N, Mercier de Lepinay B, Meyer B et al (2001). The active main Marmara fault. Earth Planet Sc Lett 192: 595-616.

Loveless JP, Meade BJ (2011). Partitioning of localized and diffuse deformation in the Tibetan Plateau from joint inversions of geologic and geodetic observations. Earth Planet Sc Lett 303: 11-24.

Lundgren P, Giardini D, Russo RM (1998). Geodynamic framework for eastern Mediterranean kinematics. Geophys Res Lett 25: 4007-4010.

Lyberis N (1984). Tectonic evolution of the North Aegean trough. Geol Soc Spec Publ 17: 709-725.

Mardia KV (1972). Statistics of Directional Data. London, UK: Academic Press.

Mascle J, Benkhelil J, Bellaiche G, Zitter T, Woodside J, Loncke L, Party PIS (2000). Marine geologic evidence for a Levantine-Sinai plate, a new piece of the Mediterranean puzzle. Geology 28: 779-782.

Masson F, Djamour Y, Gorp SV, Chéry J, Tatar M, Tavakoli F, Nankali H, Vernant P (2006). Extension in NW Iran driven by the motion of the South Caspian Basin. Earth Planet Sc Lett 252: 180-188.

McClusky S, Balassanian S, Barka A, Demir C, Ergintav S, Georgiev I, Gürkan O, Hamburger M, Hurst K, Kahle H et al (2000). Global Positioning System constraints on plate kinematics and dynamics in the eastern Mediterranean and Caucasus. J Geophys Res 105: 5695-5719.

McKenzie D (1972). Active tectonics of the Mediterranean Region. Geophys J Roy Astr S 30: 109-185.

McKenzie D (1976). The east Anatolian fault: a major structure in eastern Turkey. Earth Planet Sc Lett 29: 189-193.

Meade B, Hager B, McClusky S, Reilinger R, Ergintav S, Lenk O, Barka A, Özener H (2002). Estimates of seismic potential in the Marmara Sea region from block models of secular deformation constrained by Global Positioning System measurements. B Seismol Soc Am 92: 208-215.

Meghraoui M, Aksoy ME, Akyüz H, Ferry M, Dikbaş A, Altunel E (2012). Paleoseismology of the North Anatolian Fault at Güzelköy (Ganos segment, Turkey): size and recurrence time of earthquake ruptures west of the sea of Marmara. Geochem Geophys Geosy 13: Q04005.

Meijer PT, Wortel MJR (1996). Temporal variation in the stress field of the Aegean region. Geophys Res Lett 23: 439-442.

Meijer PT, Wortel MJR (1997). Present-day dynamics of the Aegean region: a model analysis of the horizontal pattern of stress and deformation. Tectonics 16: 879-895.

Meijers MJM, van Hinsbergen DJJ, Dekkers MJ, Altıner D, Kaymakçı N, Langereis CG (2011). Pervasive Palaeogene remagnetization of the central Taurides fold-and-thrust belt (southern Turkey) and implications for rotations in the Isparta Angle. Geophys J Int 184: 1090-1112.

Melosh HJ, Raefsky A (1981). A simple and efficient method for introducing faults into finite element computations. B Seismol Soc Am 71: 1391-1400.

Melosh HJ, Williams CA (1989). Mechanics of graben formation in crustal rocks: a finite element analysis. J Geophys Res 94: 13961-13973.

Müller RD, Sdrolias M, Gaina C, Roest WR (2008). Age, spreading rates, and spreading asymmetry of the world's ocean crust. Geochem Geophys Geosy 9: GC001743.

Nur A, Helsley C (1971). Paleomagnetism of Tertiary and recent lavas of Israel. Earth Planet Sc Lett 10: 375-379.

Nyst M, Thatcher W (2004). New constraints on the active tectonic deformation of the Aegean. J Geophys Res 109: B11406.

Ocakoğlu N (2012). Investigation of Fethiye-Marmaris Bay (SW Anatolia): seismic and morphologic evidences from the missing link between the Pliny Trench and the Fethiye-Burdur Fault Zone. Geo-Marine Letters 32: 17-28.

Okay AI, Zattin M, Cavazza W (2010). Apatite fission-track data for the Miocene Arabia-Eurasia collision. Geology 38: 35-38.

Özbakır AD, Şengör AMC, Wortel MJR, Govers R (2013). The Pliny–Strabo trench region: a large shear zone resulting from slab tearing. Earth Planet Sc Lett 375: 188-195.

Özeren MS, Holt WE (2010). The dynamics of the eastern Mediterranean and eastern Turkey. Geophys J Int 183: 1165-1184.

Parlak O (2004). Çelikhan – Erkenek arasında Doğu Anadolu fayının özellikleri. MSc, İstanbul Technical University, İstanbul, Turkey (in Turkish).

Piper JDA, Gürsoy H, Tatar O, Beck ME, Raoa A, Koçbulut F, Mesci BL (2010). Distributed neotectonic deformation in the Anatolides of Turkey: A palaeomagnetic analysis. Tectonophysics 488: 31-50.

Piromallo C, Morelli A (2003). P wave tomography of the mantle under the Alpine-Mediterranean area. J Geophys Res 108: 2065.

Plattner C, Malservisi R, Govers R (2009). On the plate boundary forces that drive and resist Baja California motion. Geology 37: 359-362.

Polonia A, Gasperini L, Amorosi A, Bonatti E, Bortoluzzi G, Çağatay N, Capotondi L, Cormier MH, Görür N, McHugh C et al. (2004). Holocene slip rate of the North Anatolian fault beneath the Sea of Marmara. Earth Planet Sc Lett 227: 411-426.

Price SP, Scott B (1994). Fault-block rotations at the edge of a zone of continental extension; southwest Turkey. J Struct Geol 16: 381-392.

Provost AS, Chery J, Hassani R (2003). 3D mechanical modelling of the GPS velocity field along the North Anatolian fault. Earth Planet Sc Lett 209: 361-377.

Pucci S, De Martini PM, Pantosti D (2008). Preliminary slip rate estimates for the Duzce segment of the North Anatolian Fault zone from offset geomorphic markers. Geomorphology 97: 538-554.

Ranalli G (1987). Rheology of the Earth. 1st ed. Crows Nest, Australia: Allen & Unwin.

Reilinger R, McClusky S, Paradissis D, Ergintav S, Vernant P (2010). Geodetic constrains on the tectonic evolution of the Aegean region and strain accumulation along Hellenic subduction zone. Tectonophysics 488: 22-30.

Reilinger R, McClusky S, Vernant P, Lawrence S, Ergintav S, Çakmak R, Özener H, Kadirov F, Guliev I, Stepanyan R et al (2006). GPS constraints on continental deformation in the Africa-Arabia-Eurasia continental collision zone and implications for the dynamics of plate interactions. J Geophys Res 111: B05411.

Robertson A (1998). Tectonic significance of the Eratosthenes seamount: a continental fragment in the process of collision with a subduction zone in the eastern Mediterranean (Ocean Drilling Program Leg 160). Tectonophysics 298: 63-82.

Şaroğlu F, Emre Ö, Boray A (1987). Türkiye'nin diri fayları ve depremsellikleri. MTA Rap. 8174. Ankara, Turkey: MTA (in Turkish).

Şaroğlu F, Emre Ö, Kuşçu I (1992). The east Anatolian fault zone of Turkey. Annales Tectonicae 6: 99-125.

Schindler C (1997). Geology of northwestern Turkey: results of the Marmara poly-project. In: Schindler C, Pfister M, editors. Active Tectonics of Northwestern Anatolia: The Marmara Poly-Project. Zurich, Switzerland: Hochschulverlag AG, pp. 329-373.

Şengör AMC (1987). Cross-faults and differential stretching of hanging walls in regions of low-angle normal faulting: examples from western Turkey. Geol Soc Spec Publ 28: 575-589.

Şengör AMC, Özeren S, Genç T, Zor E (2003). East Anatolian high plateau as a mantle supported, north-south shortened domal structure. Geophys Res Lett 30: GL017858.

Şengör AMC, Tüysüz O, İmren C, Sakınç M, Eyidoğan H, Görür N, Le Pichon X, Rangin C (2005). The North Anatolian Fault: a new look. Annu Rev Earth Pl Sc 33: 37-112.

Şengör AMC, Yılmaz Y (1981). Tethyan evolution of Turkey: a plate tectonic approach. Tectonophysics 75: 181-241.

Seymen İ, Aydın A (1972). Bingol deprem fayı ve bunun kuzey Anadolu fayı ile iliskisi. MTA Dergisi 79: 1-8 (in Turkish).

Seyrek A, Demir T, Pringle MS, Yurtmen S, Westaway RWC, Beck A, Rowbotham G (2007). Kinematics of the Amanos Fault, southern Turkey, from Ar/Ar dating of offset Pleistocene basalt flows: transpression between the African and Arabian plates. Geol Soc Spec Publ 290: 255-284.

Shaw B, Jackson J (2010). Earthquake mechanisms and active tectonics of the Hellenic subduction zone. Geophys J Int 181: 966-984.

Stein C, Stein S (1992). A model for the global variation in oceanic depth and heat flow with lithospheric age. Nature 359: 123-129.

Tapponnier P, Ryerson FJ, Van der Woerd J, Meriaux AS, Lasserre C (2001). Long-term slip rates and characteristic slip: keys to active fault behaviour and earthquake hazard. Cr Acad Sci II A 333: 483-494.

Taymaz T, Jackson JA, Westaway R (1990). Earthquake mechanisms in the Hellenic trench near Crete. Geophys J Int 102: 695-731.

Tchalenko JS (1970). Similarities between shear zones of different magnitudes. Geol Soc Am Bull 81: 1625-1640.

Ten Veen JH, Woodside J, Zitter T, Dumont J, Mascle J, Volkonskaia A (2004). Neotectonic evolution of the Anaximander Mountains at the junction of the Hellenic and Cyprus arcs. Tectonophysics 391: 35-65.

Tesauro M, Kaban MK, Cloetingh SAPL (2009). A new thermal and rheological model of the European lithosphere. Tectonophysics 476: 478-495.

Thatcher W (2009). How the continents deform: the evidence from tectonic geodesy. Annu Rev Earth Pl Sc 37: 237-262.

Tiryakioğlu İ, Floyd M, Erdoğan S, Gülal E, Ergintav S, McClusky S, Reilinger R (2013). GPS constraints on active deformation in the Isparta Angle region of SW Turkey. Geophys J Int 195: 1455-1463.

Turan M (1993). Some important tectonic structures in the surroundings of elazig and their meaning in the geological evolution of the region. In: Proceedings of Suat Erk Symposium, Ankara University, Ankara, Turkey, pp. 193-204.

Van Benthem S, Govers R (2010). The Caribbean plate: pulled, pushed, or dragged? J Geophys Res 115: B10409.

Van Dongen P, Van der Voo R, Raven T (1967). Paleomagnetism and the Alpine tectonics of Eurasia III: paleomagnetic research in the Central Lebanon Mountains and in the Tartous area (Syria). Tectonophysics 4: 35-53.

Van Hinsbergen DJJ, Langereis CG, Meulenkamp JE (2005). Revision of the timing, magnitude and distribution of Neogene rotations in the western Aegean region. Tectonophysics 396: 1-34.

Van Hinsbergen D, Schmid S (2012). Map-view restoration of the Aegean back-arc. Tectonics 31: 1-101.

Vernant P, Reilinger R, McClusky S (2014). Geodetic evidence for low coupling on the Hellenic subduction plate interface. Earth Planet Sc Lett 385: 122-129.

Vidal N, Alvarez-Marron J, Klaeschen D (2000). The structure of the Africa-Anatolia plate boundary in the eastern Mediterranean. Tectonics 19: 723-739.

Warners-Ruckstuhl KN, Govers R, Wortel R (2012). Lithosphere-mantle coupling and the dynamics of the Eurasian plate, Geophys J Int 189: 1253-1276.

Warners-Ruckstuhl KN, Govers R, Wortel R (2013). Tethyan collision forces and the stress field of the Eurasian Plate. Geophys J Int 195: 1-15.

Watts AB, Zhong S (2000). Observations of flexure and the rheology of oceanic lithosphere. Geophys J Int 142: 855-875.

Wdowinski S, Ben-Avraham Z, Arvidsson R, Ekström G (2006). Seismotectonics of the Cyprian Arc. Geophys J Int 164: 176-181.

Wessel P, Smith WHF (1998). New, improved version of Generic Mapping Tools released. EOS T Am Geophys Un 79: 579.

Westaway R (1994). Present-day kinematics of the Middle East and eastern Mediterranean. J Geophys Res 99: 12071-12090.

Westaway R, Arger J (1996). The Golbaşı basin, southeastern Turkey: a complex discontinuity in a major strike-slip fault zone. J Geol Soc London 153: 729-743.

Woodside JM, Mascle J, Zitter TAC, Limonov AF, Ergün M, Volkonskaia A, Shipboard Scientists of PRISMED II Expedition (2002). The Florence Rise, the western bend of the Cyprus arc. Mar Geol 185: 177-194.

Wortel R, Spakman W, Govers R (2006). Deep structure and evolution of the Cyprus arc. Geophys Res Abs 8: 07892.

Wright TJ, Parsons B, England PC, Fielding EJ (2004). InSAR observations of low slip rates on the major faults of western Tibet. Science 305: 236-239.

Yönlü O, Altunel E, Karabacak V, Akyüz HS (2012). Evolution of the Gölbaşı basin and its implications for the long-term offset on the east Anatolian fault zone, Turkey. J Geodyn 65: 272-281.

Zabcı C (2012). The 5 ka morphochronological slip-rate history and the paleoseismicity of the Ilgaz – Karlıova section of the North Anatolian Fault, Turkey. PhD, İstanbul Technical University, İstanbul, Turkey.

Zitter T, Woodside J, Mascle J (2003). The Anaximander Mountains: a clue to the tectonics of southwest Anatolia. Geol J 38: 375-394.

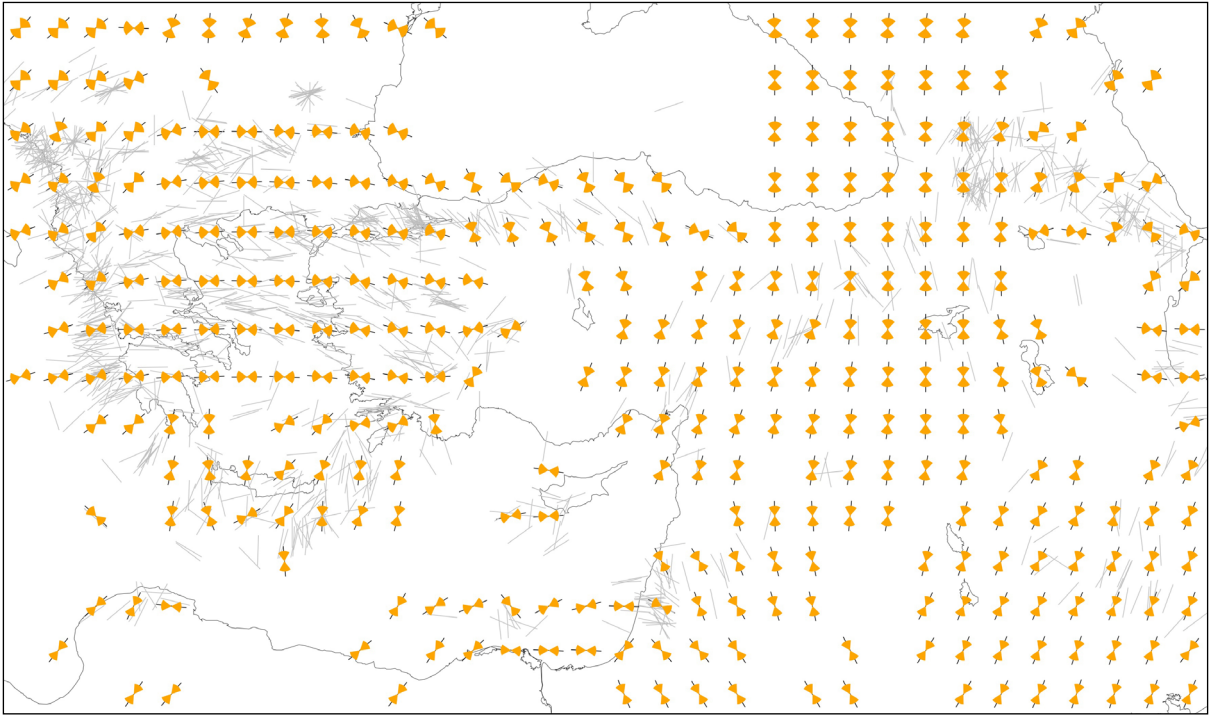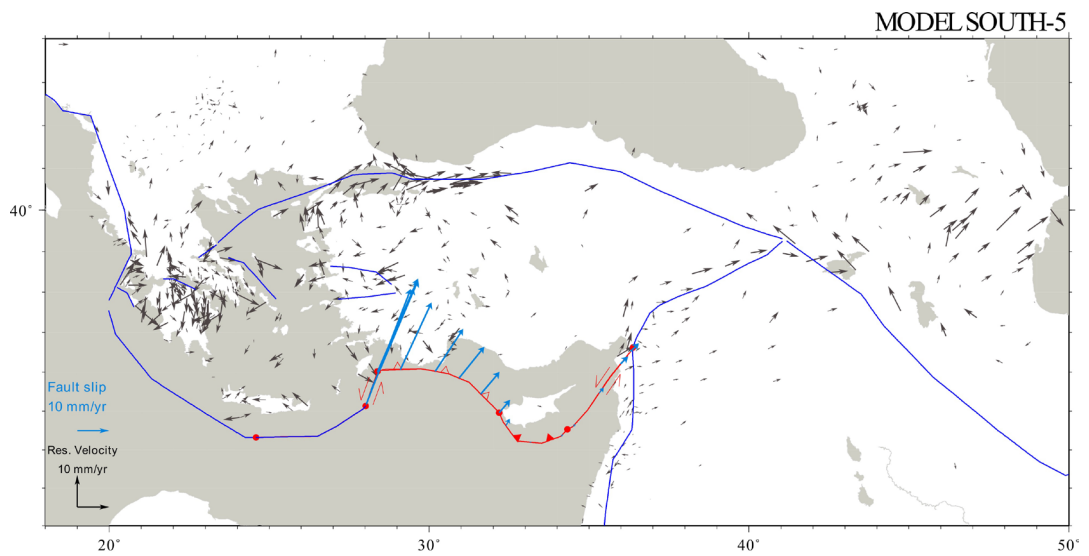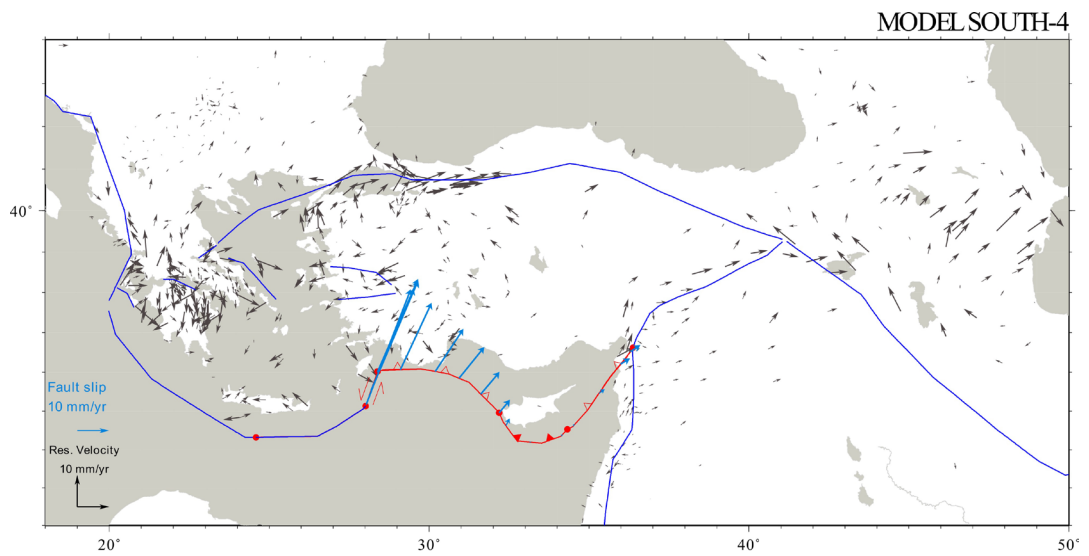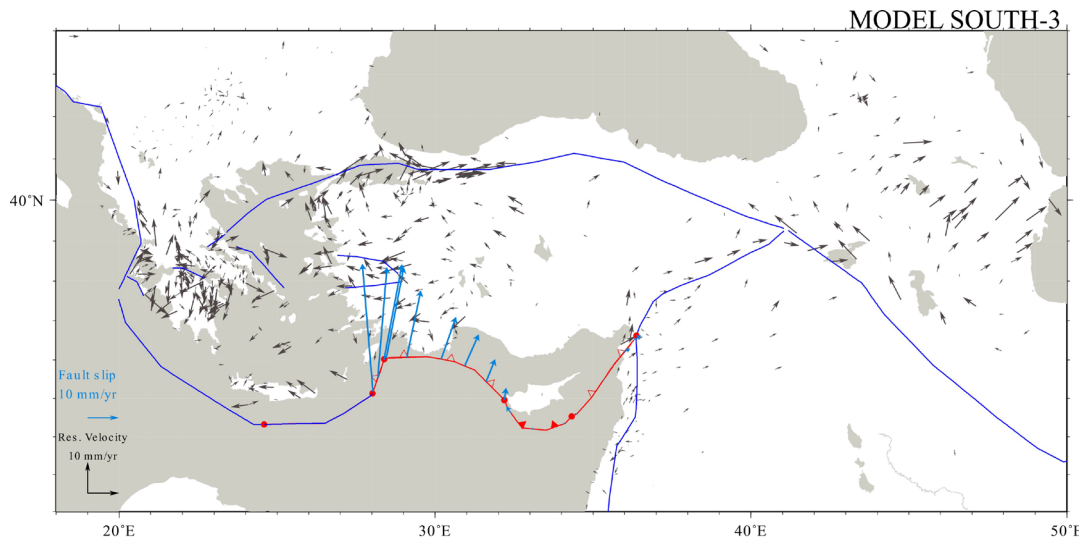**Appendix A.** WSM 2008 data, smoothed stress field and stress variances.

Figure A1. World stress map data, smoothed stress field, and stress variances.

Appendix B. Additional SOUTH model results.

MODEL SOUTH-3

MODEL SOUTH-4
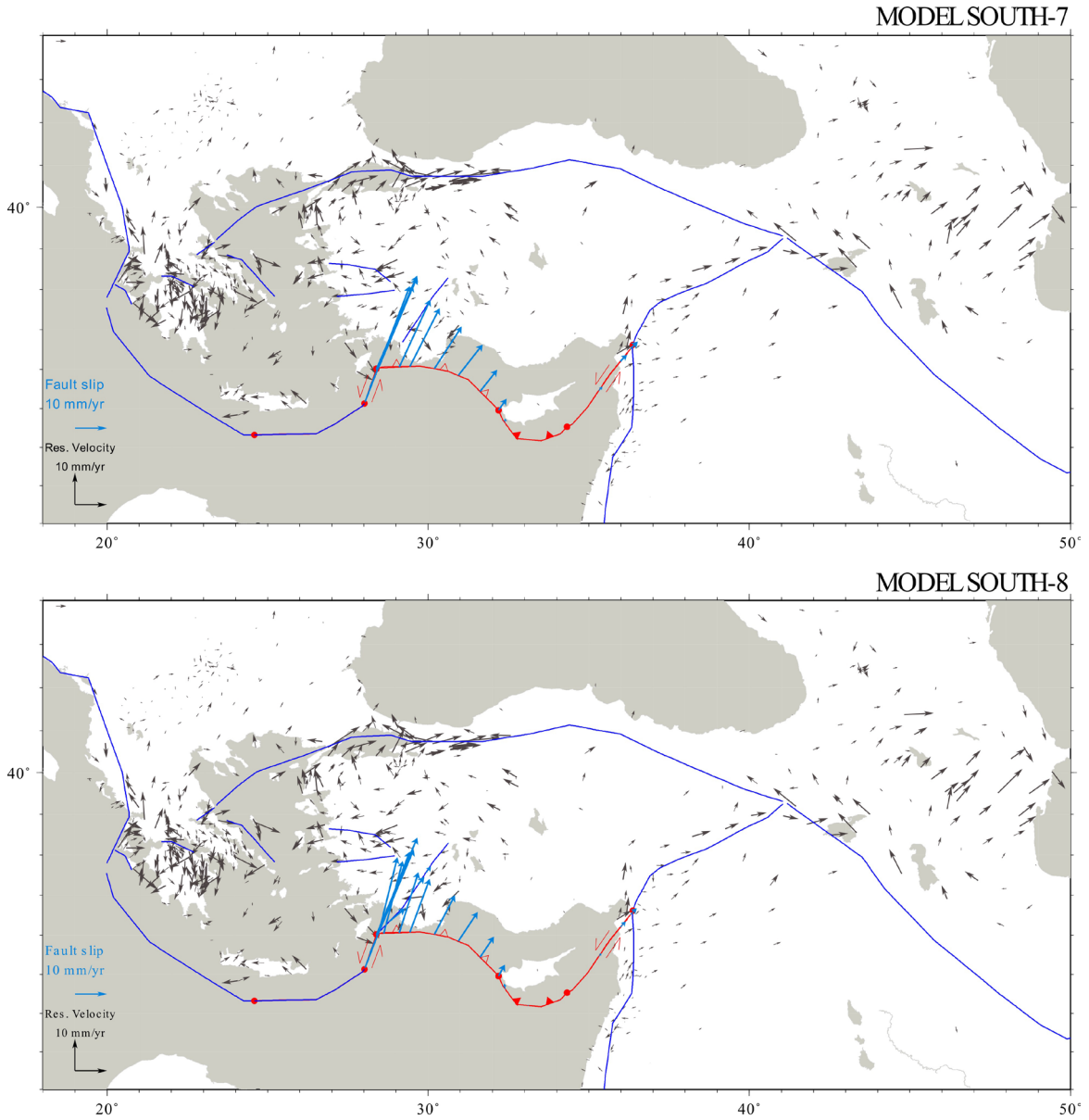
MODEL SOUTH-5

MODEL SOUTH-7

MODEL SOUTH-8

Figure B1. Velocity misfits (observed minus calculated) for a range of SOUTH models. The assumed nature of the faults is indicated on the misfit maps; filled triangles indicate that only fault-perpendicular motion is allowed and strike-slip symbols indicate that only fault parallel motion is allowed. Open triangles indicate that both strike-slip and fault normal motions are allowed in the model. Blue arrows indicate the resulting fault slip-rate and direction. a) Model SOUTH-3 with friction and down-dip relative motion only on the Cyprus trench; b) Model SOUTH-4 with strike-slip only on the Rhodes plate boundary segment; c) Model SOUTH-5 with strike-slip only on the Latakia segment of the plate boundary; d) Model SOUTH-7 with onshore Burdur–Fethiye fault, not connected to Pliny-Strabo trenches; e) Model SOUTH-8 with Burdur–Fethiye fault connected to Pliny-Strabo trenches.

Appendix C. Geodetic slip-rate model results for EAF and DSF.

Slip-rates for the NORTH and SOUTH model bundles for the EAF and DSF are shown in Figures C1 and C2, respectively, with results from previous model studies. For the EAF, model rates span an average of 7 ± 1 mm/year in the east and 6 ± 3 mm/year in the eastern part.

The block model of Reilinger et al. (2006), InSAR observations from Cavalie and Jonsson (2014), and the fracture mechanics model of Flerit et al. (2004) predict much higher fault slip-rates; none of them, however, agree with the long-term (geological) slip-rate data (Figure 10c), which are overestimated by ~5 mm/year. The seismic slip-rate estimates (Table 3, light blue bar at the right end of plot area) span a range of 6–10 mm/year for the EAF and represent a slip-rate value for the whole fault zone, which agrees with our results and with the geological estimates.

For the DSF, we predict model slip-rates ranging from 2 mm/year to the south to 5.5 mm/year to the north of the fault system (Figure C2). The NORTH and SOUTH model bundles have much smaller spread, indicating low sensitivity of the DSF to changing DOFs of southern boundary segments under consideration. Our model rates are smaller than those of other short-time scale studies (Flerit et al., 2004; Reilinger et al., 2006) covering this fault, but they agree with the seismic slip-rate estimates.
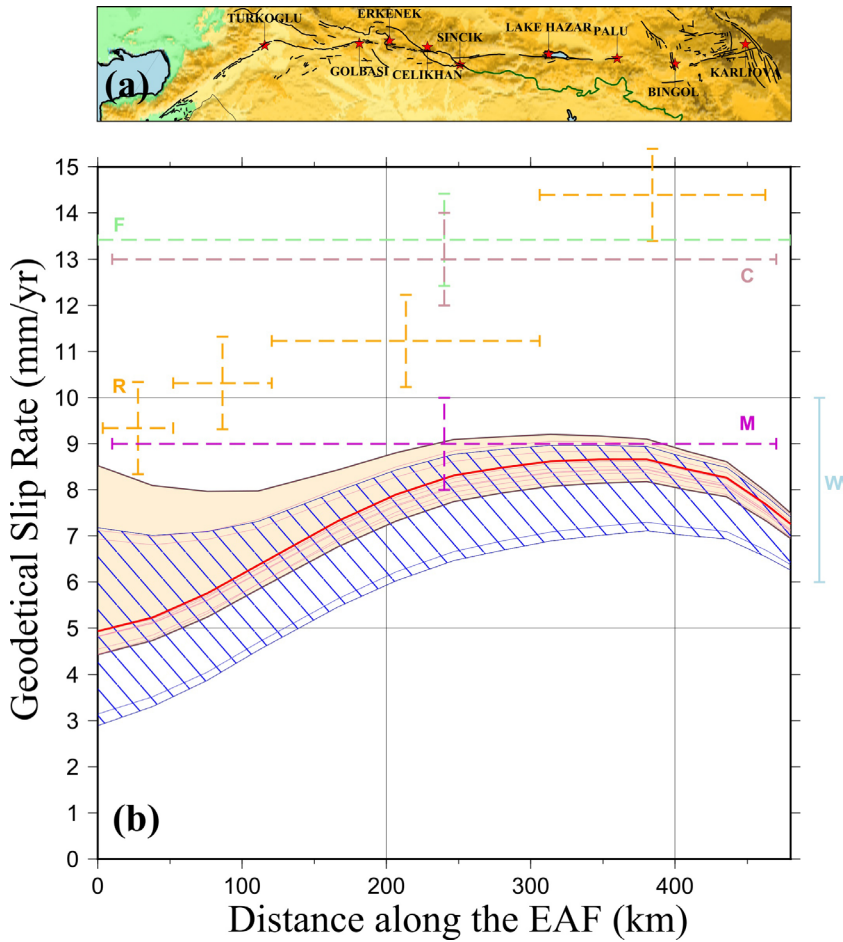

Figure C1. Comparison of geodetic slip-rates with model results for the EAF for SOUTH (orange shaded band) and NORTH (blue hachured band) models, with individual model slip-rate results shown with red and blue lines, respectively. The thick red line represents our best model (SOUTH-6). Error bars indicate previous studies: W: Westaway, 1994; M: McClusky et al., 2000; F: Flerit et al., 2004; R: Reilinger et al., 2006; C: Cavalie and Jonsson, 2014.
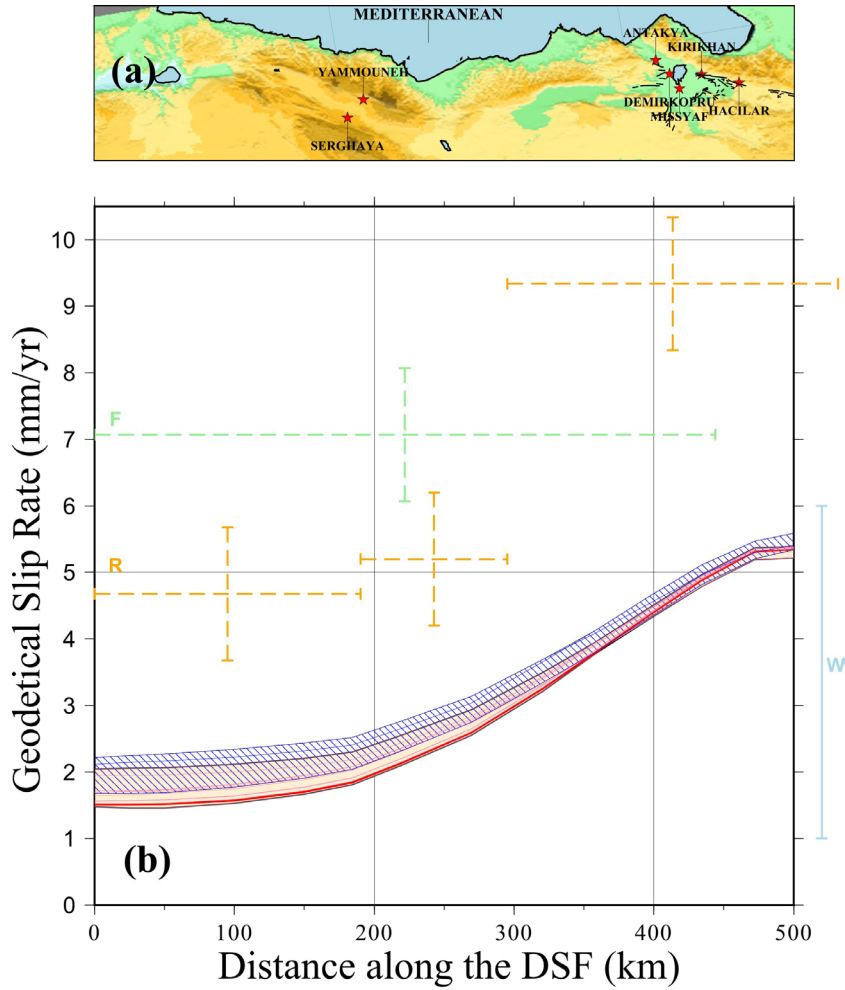
Figure C2. Model slip-rates of the DSF for both SOUTH (orange shaded band) and NORTH (blue hachured band), with individual model slip-rate results shown with red and blue lines, respectively. The thick red line represents the best model (SOUTH-6). Model slip-rates are calculated for the northern branch of the NAF, whose geometry is given nearly parallel to the plot axis shown in the upper panel. Error bars indicate previous studies: W: Westaway, 1994; M: McClusky et al., 2000; F: Flerit et al., 2004; R: Reilinger et al., 2006; C: Cavalie and Jonsson, 2014.
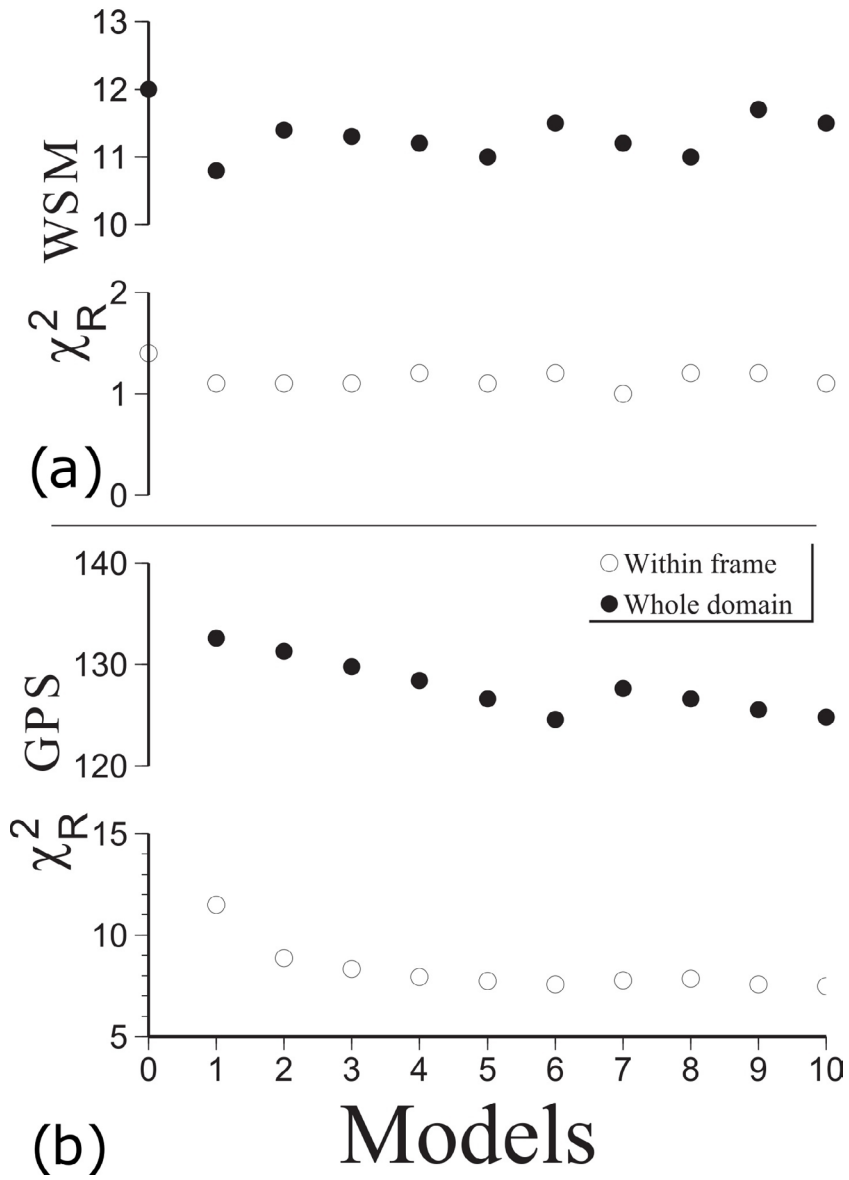
Figure C3. X_R^2 statistic computed for data points within the whole domain (filled circles) and red frame (empty circles) indicated in Figure 1 for a) model stress directions vs. World Stress Map data; b) model velocity predictions vs. GPS-derived velocity data.

Appendix D. Sensitivity of model results to boundary conditions.

In previous models of continental deformation of the Anatolia-Aegean region, GPE is included in some (Cianetti et al., 2001; Jimenez-Munt and Sabadini, 2002; Jimenez-Munt et al., 2003; Fischer, 2006; Özeren and Holt, 2010) and not in others (Meijer and Wortel, 1997; Lundgren et al., 1998; Flerit et al., 2004). All studies match model predictions to (subsets of) available data, but model results (specifically, forces and rheology) differ substantially. For instance, Özeren and Holt (2010) determined pull forces along the Hellenic trench that are about half the magnitude of those obtained by Cianetti et al. (2001). Viscosities for the Anatolia region of Fischer (2006) are two orders of magnitude lower than those of Özeren and Holt (2010). Moreover, Jimenez-Munt and Sabadini (2002) inferred that GPE-derived forces are not important for the regional kinematics, which seems at odds with Cianetti et al. (2001), Fischer (2006), and Özeren and Holt (2010). Such inconsistencies arise from the fact that GPE-based calculations require information about the density layering and mechanical properties of the lithosphere, and this information has significant uncertainties or is even absent in parts of our region of study. Uncertainties in crustal thickness and surface heat flow both contribute to significant uncertainties in the thermal structure of the lithosphere, which translates into significant uncertainties in both the forcing (via density structure) and mechanical properties (via temperature activated viscosity). Another factor contributing to uncertainties in mechanical properties is the (poorly known) composition of the crust. The last unknown is the contribution to the GPE by dynamic topography (e.g., Warners-Ruckstuhl et al., 2012, 2013).

D1. Average viscosity

We estimate the vertically averaged viscosity η of a lithospheric column by assuming that it behaves as a Newtonian fluid:

$$\eta = \frac{\int_L (\sigma_1 - \sigma_3) dz}{\int_L (\dot{\varepsilon}_1 - \dot{\varepsilon}_3) \, dz}$$

Here, $(\sigma_1 - \sigma_3)$ is differential stress and $(\dot{\varepsilon}_1 - \dot{\varepsilon}_3)$ is differential strain rate (difference between maximum and minimum eigenvalues of the corresponding tensors), and L is the lithosphere thickness (Ranalli, 1987). A common assumption is that surface strain rates are uniform throughout the lithosphere, such that lithospheric averages follow directly from differentiating (surface) geodetic velocities:

$$\eta = \frac{\frac{1}{L}\int_L (\sigma_1 - \sigma_3) dz}{(\dot{\varepsilon}_1 - \dot{\varepsilon}_3)}$$

We use surface differential strain rates for our region from Kreemer et al. (2003). Rock strength constitutes an upper limit to the differential stress it may support. An upper limit to average viscosities (and viscosity contrasts) can therefore be derived from the average lithospheric strength map of Tesauro et al. (2012) – this defines the numerator. A lower limit to average viscosities can be estimated by assuming that the average differential stress in the domain is small; we assume 1 MPa.

We use a range of viscosities of 3–5 $\times$ 10^{21} Pa s for the Anatolian-Aegean lithosphere in our sensitivity analysis to assess the dependence of model velocity results on the rheology. The Maxwell relaxation time (τ_M) for the highest viscosity domain is 330 kyr. Steady state is generally achieved after $5\tau_M$ (Plattner et al., 2009). Our viscoelastic model reached steady state around $5\tau_M$ and we output the velocities at that time.

D2. GPE-derived horizontal forces

GPE forces are applied inside the computational domain. We use the crustal thickness and densities from the CRUST2.0 model (Bassin et al., 2000) and topographical height from the ETOPO2 dataset (2-Minute Gridded Global Relief Data, http://www.ngdc.noaa. gov/mgg/fliers/06mgg01.html). The oceanic lithosphere of the Mediterranean is older than 180 Ma (Müller et al., 2008), and hence we assume that the conductive cooling produced a linear geotherm (Stein and Stein, 1992). Mantle lithospheric density profiles are constructed as a function of a linear geotherm for the continental lithosphere. Two different GPE values can be calculated from two end-member density interface topologies: 1) a compensated mantle lithosphere density profile with equalized pressure at the base of the lithosphere and 2) uncompensated pressures at the base. The latter assumption induces about 30%–50% larger forces for this region due to lateral density variations. Ghosh et al. (2009) inferred 10%–20% larger forces from their uncompensated global model with respect to the compensated one. Lithospheric thickness is assumed to be 100 km, since there are no cratonic areas in the model domain where the buoyancy from such cratonic roots would affect the GPE calculations.

Given these uncertainties, we investigate end-members for both the GPE-derived forces and for the viscosities in our region of interest. We adopt the plate boundaries and faults of our preferred model (SOUTH-6) from the previous section with one important exception; the Hellenic trench and Pliny-Strabo faults are represented as frictionless faults that can slip in response to model stresses.

Global plate tectonics is driven by body forces, which are manifested within the plates by GPE-derived forces. In a regional model like ours (Figure D1), boundary conditions ideally would be an accurate representation of GPE-derived forces that surrounding regions exert on the model domain. To determine such boundary conditions is a formidable problem in itself, mostly because the continuity of stresses (and thus forces) across plate boundaries and major faults is strongly modulated by relative details at these discontinuities (e.g., De Franco et al., 2008a, 2008b). Assuming that GPE within the model domain does not significantly affect the velocities of major plates, we impose boundary forces proportional to observed plate velocities along the Africa, Arabia, and Europe margins. Motivated by the results of a recent stress modeling study (Warners-Ruckstuhl et al., 2013) that indicated that GPE forces generated beyond our E and NW domain boundaries are not transmitted into our region of interest, we do not impose forces along these boundaries. A significant difference from the previous models is thus that we do not impose differential velocities/forces at the Hellenic trench.

D3. Results of GPE forcing models

Figure D2 summarizes the results of our end-member GPE-models. Figure D2a demonstrates that the misfit is particularly large in the eastern portion of the trench. Here, model SOUTH-6 yields a better (albeit not perfect) match to the observations as a result of additional (subduction-related?) forcing along the Hellenic trench in this model. For the region east of 31°E, Figure D2b shows an acceptable fit to the GPS velocity magnitudes of the GPE-driven models with low-end viscosities. Importantly, the fit of model SOUTH-6 is equally good, indicating that the representation by edge forces of (distributed) GPE forces does not affect the result. To the west of 31°E, i.e. closer to the Hellenic trench, the misfit between the GPE-driven models and observations is significant. Our conclusion of the previous section, that model SOUTH-6 matches the geodetic observations best, is thus not affected by our choice of boundary conditions in boundary-driven models.
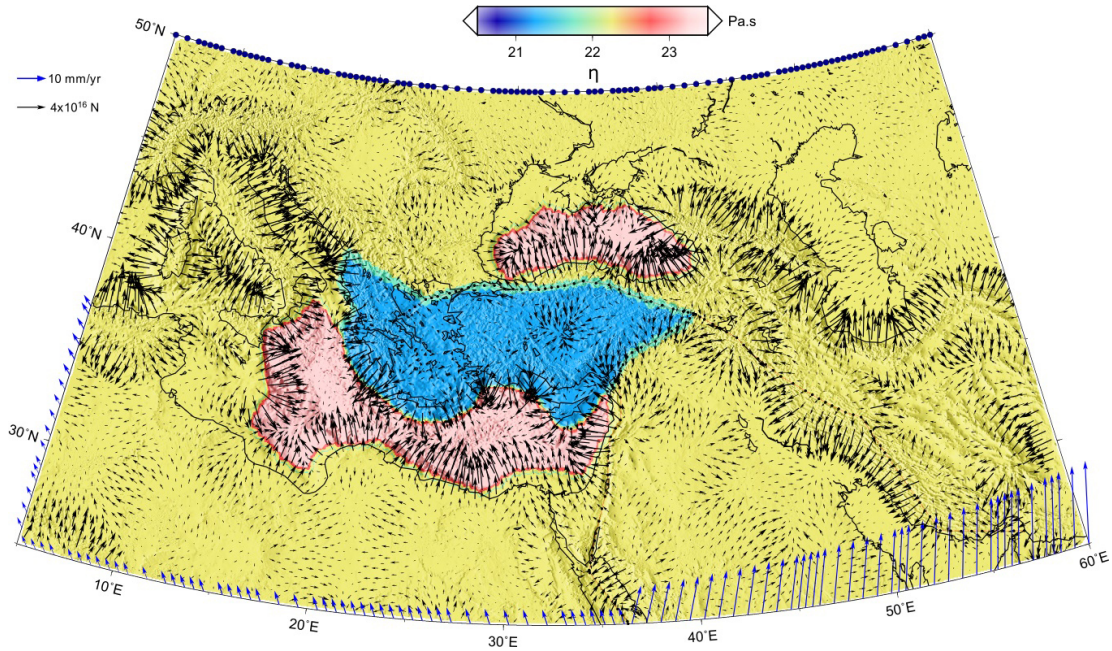

Figure D1. Model domain and boundary conditions (blue arrows) of GPE-driven models. The specific model shown here is for relatively low Aegean-Anatolian viscosity, and for horizontal forces (black arrows) computed with the assumption that the lithosphere is not isostatically compensated. Logarithmic viscosity contours are draped over shaded relief.
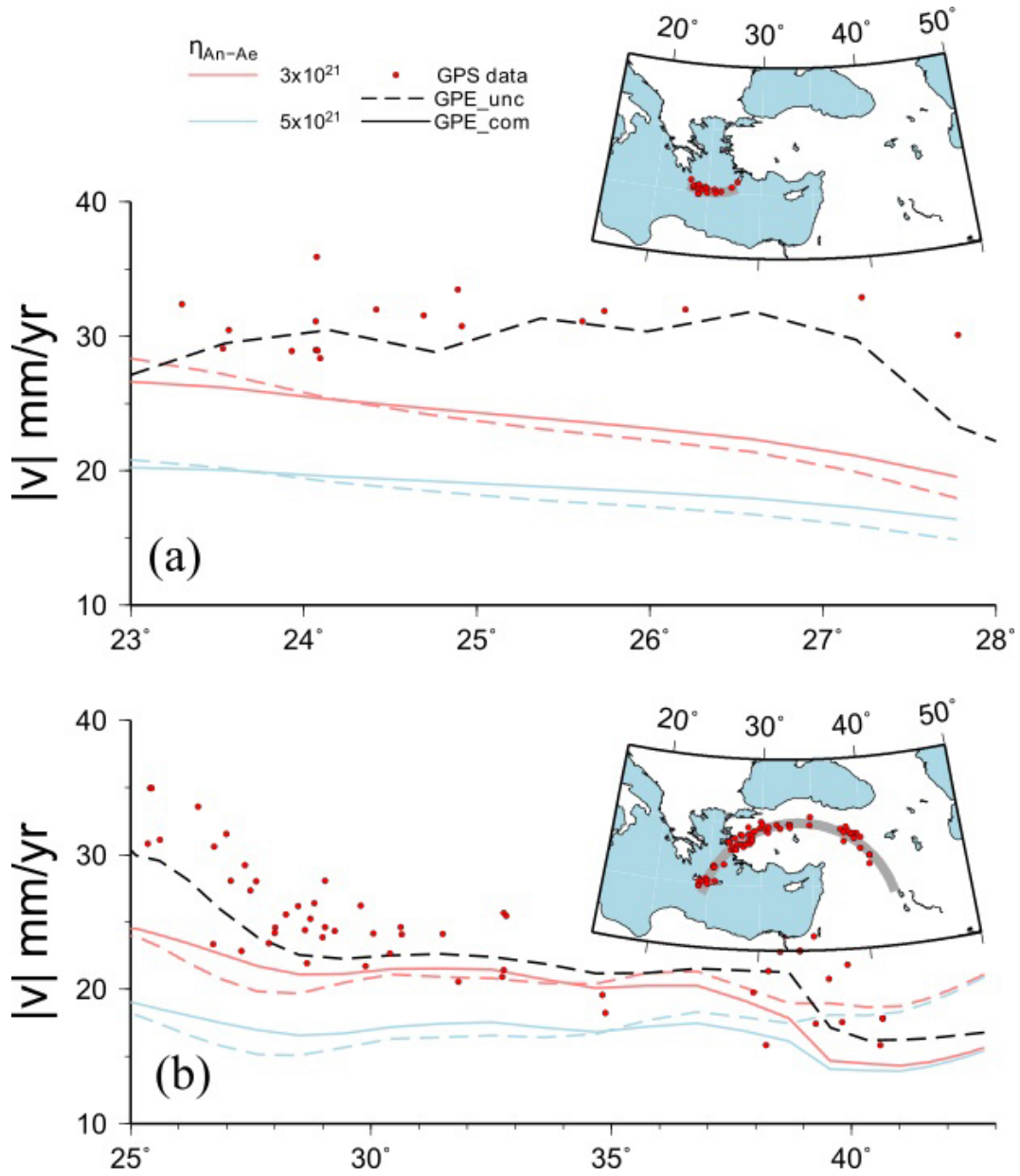
Figure D2. Comparison of observed velocity magnitudes with results of a range of GPE-driven models. Solid lines result from GPE forces derived from isostatically compensated lithosphere, dashed lines from uncompensated lithosphere (see Appendix D for details). Red and blue lines are results of models for relatively low and high viscosities of the Aegean-Anatolian region, respectively. Black dashed lines show velocity magnitudes from model SOUTH-6. a) Velocities in a swath (inset) along the Hellenic trench. b) Velocities along a swath (inset) that is approximately parallel to the relative motion direction of Anatolia with respect to Europe.